MULTISCALE MODEL. SIMUL.
Vol. 8, No. 4, pp. 1212–1243

A NEW POTENTIAL REGULARIZATION OF THE ONE-DIMENSIONAL EULER AND HOMENTROPIC EULER EQUATIONS*

GREG NORGARD† AND KAMRAN MOHSENI‡

Abstract. This paper examines an averaging technique in which the nonlinear flux term is expanded and the convective velocities are passed through a low-pass filter. It is the intent that this modification to the nonlinear flux terms will result in an inviscid regularization of the homentropic Euler equations and Euler equations. The physical motivation for this technique is presented and a general method is derived, which is then applied to the homentropic Euler equations and Euler equations. These modified equations are then examined, revealing that they share conservative properties, shock speeds, and traveling wave solutions with the original equations. If compactness of the solutions is assumed, then it can be proven that as the averaging is diminished the solutions converge to weak solutions of the original equations. Finally, numerical simulations are conducted showing that the modified equations appear regularized and converge to the entropy solution in shock tube simulations.

Key words. shock regularization, low-pass filter, spatial averaging, conservation law, Euler equations, Lagrangian averaging, turbulence modeling

AMS subject classifications. 76N10, 76L05, 35Q35, 35Q31, 35L60, 35L65, 35L67

DOI. 10.1137/090763640

1. Introduction.

This paper examines a modification of the homentropic Euler and Euler equations where the flux term is expanded and the convective velocities are passed through a low-pass filter. It is the intent that this modification to the nonlinear flux terms will result in an inviscid regularization of the homentropic Euler equations and Euler equations. The ultimate goal with this regularization is to develop a proper modeling of small scale behavior so that both shocks and turbulence can be captured in one comprehensive technique.

This paper first describes the proposed regularizing method and investigates the shock speeds and the conservative effects of the modified equations. Then this method is applied to the one-dimensional homentropic Euler equations and the one-dimensional Euler equations. Preliminary analytical results are established regarding the modified Euler equations. Then using numerical techniques we demonstrate the convergence of the solutions of the regularized equations to the entropy solution of a shock tube problem.

The inspiration for this new technique comes from recent work done on a similarly modified Burgers equation. The Burgers equation, $u_t + uu_x = 0$, is considered a simplistic model of compressible flow which forms shocks readily. Classically, this equation is regularized with a dissipative term, such as viscosity or hyperviscosity. Additionally, Burgers equation can be regularized with linear dispersion resulting in the KdV equations; however, this regularization will not result in a convergence to an

*Received by the editors July 1, 2009; accepted for publication (in revised form) March 16, 2010; published electronically July 1, 2010. The research in this paper was partially supported by the AFOSR contract FA9550-09-1-0158.

http://www.siam.org/journals/mms/8-4/76364.html

†Department of Applied Mathematics, University of Colorado, Boulder, CO 80309 (gregory.norgard@colorado.edu).

‡Aerospace Engineering Sciences, Department of Applied Mathematics, University of Colorado, Boulder, CO 80309 (mohseni@colorado.edu).

entropy solution. Recently, work has been done by our group and others investigating a regularization of the Burgers equation where the nonlinear term is manipulated by averaging the convective velocity [1, 2, 3, 4, 5, 6, 7],

$$u_t + \bar{u}u_x = 0, \tag{1.1a}$$

$$\bar{u} = g^\alpha * u, \tag{1.1b}$$

$$g^\alpha = \frac{1}{\alpha} g\left(\frac{x}{\alpha}\right), \tag{1.1c}$$

where g is an averaging kernel, with emphasis on the Helmholtz filter. In this paper we extend this technique to the homentropic Euler and Euler equations.

1.1. History of α-regularization of Burgers equations. The technique used on the Burgers equations has been thoroughly investigated and established as a valid shock regularization technique. Bhat and Fetecau proved using the Helmholtz filter that solutions to equations (1.1) exist and are unique [3]. They went on to show that a subsequence of the solutions will converge to a weak solution of the Burgers equation and presented numerical evidence that it converges to the entropy solution. Pavlova also demonstrated numerical evidence for the convergence to the entropy solution for equations (1.1) equipped with a Helmholtz filter [7]. Norgard and Mohseni went on to establish the existence and uniqueness of the solutions to a multiple-dimensional version of the equations for a wide variety of filters, and that when the initial conditions are C^1, the solution remains C^1 for all time [2]. Later they were able to prove that for bell-shaped initial conditions, converging subsequences of the solutions to equations (1.1) converge to the entropy solution of the inviscid Burgers equation as $\alpha \to 0$ [5, 8], also providing evidence that this holds true for all continuous initial conditions. These analytical results, along with multiple numerical results, regarding shock thickness and energy decay results have shown that this is a valid shock regularization technique.

1.2. Other α-regularizations. Work on the regularization of the Burgers equation was inspired by and related to work done on the Lagrangian averaged Navier–Stokes (LANS-α) equations [9, 10, 11, 12, 13, 14, 15, 16, 17]. The LANS-α equations also employ an averaged velocity in the nonlinear term and have been successful in modeling some turbulent incompressible flows.

Additional α-regularizations also appear in incompressible Euler equations and vortex regularization [18, 19], magnetic hydrodynamics [20], Schrödinger's equations [21], and trajectory attractors in the Navier–Stokes equations [22]. These types of regularizations are appearing to be quite beneficial.

It is thought that a similar regularization could be accomplished for equations that describe compressible flow. Encouraged by the results for the Burgers equation, the next step is to attempt to introduce averaging into the one-dimensional homentropic Euler equations, a simplified version of the full Euler equations, where pressure is purely a function of density. There have been several attempts at such a regularization.

Inspired by the existence and uniqueness proofs from the averaged Burgers equations [2, 3], Norgard and Mohseni [23] averaged the characteristics of the homentropic Euler equations to derive the equations

$$\rho_t + \bar{u}\rho_x + \rho\frac{\bar{a}}{a}u_x = 0, \tag{1.2a}$$

$$u_t + \bar{u}u_x + \frac{a\bar{a}}{\rho}\rho_x = 0, \tag{1.2b}$$

$$\bar{u} = g * u, \tag{1.2c}$$

$$\bar{a} = g * a, \tag{1.2d}$$

with $a^2 = \gamma\rho^{\gamma-1}$. While these equations were proven to have a convenient existence and uniqueness proof, they were ultimately found to have significant departures in behavior from the homentropic Euler equations, specifically for the Riemann problem. It was discovered that when the characteristics are averaged, there was no creation or destruction of characteristics. A shock in homentropic Euler equations can produce new characteristics in one of the Riemann invariants. The new equations do not capture this behavior and result in departures from the desired behavior.

Using a Lagrangian averaging technique, Bhat and Fetecau [24] derived the following equations:

$$\rho_t + (\rho u)_x = 0, \tag{1.3a}$$

$$w_t + (uw)_x - \frac{1}{2}(u^2 + \alpha^2 u_x^2)_x = -\frac{p_x}{\rho}, \tag{1.3b}$$

$$\rho w = \rho v - \alpha^2 \rho_x u_x, \tag{1.3c}$$

$$v = u - \alpha^2 u_{xx}. \tag{1.3d}$$

While the solutions to the system remained smooth and contained much structure, it was found that the equations were "not well-suited for the approximation of shock solutions of the compressible Euler equations" [24].

Another attempt by Bhat, Fetecau, and Goodman used a Leray-type averaging [25] leading to the equations

$$\rho_t + \bar{u}\rho_x + \rho u_x = 0, \tag{1.4}$$

$$u_t + \bar{u}u_x + \frac{p_x}{\rho} = 0, \tag{1.5}$$

$$u = \bar{u} - \alpha^2 \bar{u}_{xx}, \tag{1.6}$$

with $p = \kappa\rho^{\gamma}$. They then showed that weakly nonlinear geometrical optics (WNGO) asymptotic theory predicts that the equations will have global smooth solutions for $\gamma = 1$ and form shocks in finite time for any other value of γ; namely, $\gamma \neq 1$, again not representing the behavior of the compressible Euler equations.

Additionally in 2005, Bhat et al. [26] applied the Lagrangian averaging approach to the full compressible Euler equations. Their approach successfully derived a set of Lagrangian averaged Euler (LAE-α) equations. However, these equations were quite long and complicated, and it seemed that numerical simulations involving these equations would be impractical for real-world applications.

This paper proposes a new technique that appears to regularize the homentropic Euler and Euler equations and begins a preliminary investigation of the proposed method that yields various analytic and numerical results that are, thus far, encouraging. We show that the original conserved quantities are preserved and that shock speeds are consistent with the original equations. While the existence of smooth solutions is not proven, numerical experiments are conducted that suggest smooth solutions. Section 2 details the motivation behind the technique, with section 4 detailing the general method. Section 3 specifies the averaging kernels that we consider in our technique. Section 7 examines the modified homentropic Euler equations looking at conservation of mass and momentum, traveling wave solutions, eigenvalues,

and convergence to weak solutions of the original homentropic Euler equations, and finally examines some numerical results. Section 8 examines the same properties, but with the modified Euler equations. All is then followed by concluding remarks and descriptions of relevant open questions.

2. Motivation. The motivation for our technique stems from a simple concept: that nonlinear terms generate high wave modes continuously as time progresses. Consider the mechanics behind shock formation and turbulence. The nonlinear convective term $\mathbf{u} \cdot \nabla \mathbf{u}$ generates high wave modes by transferring energy into smaller scales as time progresses. This nonlinear term is found in the Burgers equations where it causes nonlinear steepening, resulting in shocks. It is also found in the Euler and Navier–Stokes equations where it generates high wave modes by tilting and stretching vortices [27]. Thus this nonlinear term is cascading energy down into smaller and smaller scales. In the three-dimensional Navier–Stokes and three-dimensional Euler equations, the energy cascade has a slope of $-\frac{5}{3}$ until reaching the Kolmogorov scale, illustrated in Figure 2.1(a). The Burgers equation has an energy cascade slope of -2 until viscosity begins to dominate, seen in Figure 2.1(b) [28, 29]. It is by reducing this cascade of energy after some length of scale that we intend to regularize the Euler equations. In the Burgers equation the nonlinear term uu_x was replaced with $\bar{u}u_x$. A low-pass filtered velocity will have less energy in its high wave modes after the scale $\frac{1}{\alpha}$. Thus when inserted into the nonlinear term, the energy cascade will be lessened. This modification to the Burgers equations was found to result in a regularization of the equations. It is our hypothesis that a similar modification to the Euler equations will have similar results.

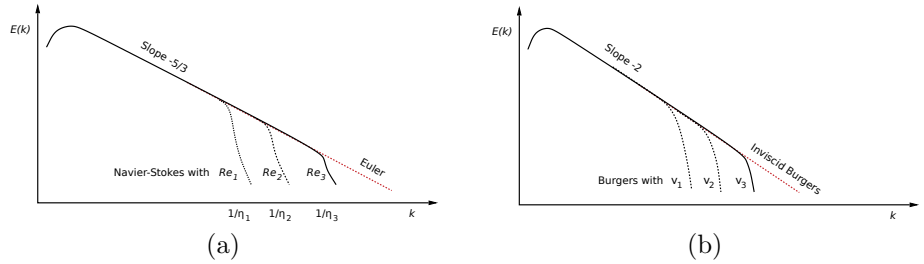

FIG. 2.1. *Schematics of energy cascade for the Navier–Stokes/Euler equations and the viscous/inviscid Burgers equation are shown. In an inviscid flow, both turbulence and shocks show continuous generation of higher wave modes indefinitely.* (a) *Energy cascades from high wavelengths to lower wavelengths at a predicted rate of* $-\frac{5}{3}$ *for the Navier–Stokes/Euler equations. For the Navier–Stokes equations, the kinetic energy drops drastically upon reaching a certain wavelength—the Kolmogorov scale,* η*. For the Euler equations the cascade continues indefinitely. Here* $Re_1 < Re_2 < Re_3$. (b) *For the Burgers equation, shocks can form from continuous initial conditions. The energy cascade has a slope of* -2 *when shocks form, until viscosity begins to exert its influence and balance the steepening effect of the nonlinear term. Here* $\nu_3 < \nu_2 < \nu_1$.

3. Averaging kernels. In our previous work [2, 5] the low-pass filters were assumed to have certain properties. As an averaging kernel, it seems intuitively reasonable that an averaging should give no negative weight, have no directional preference, and give higher weight to other particles that are physically closer. Mathematically this is equivalent to saying that the convolution kernels g are assumed to be normalized, nonnegative, decreasing, and even. This is summarized in Table 3.1. The physical rationale behind these properties is described more thoroughly in our previous work [2] when dealing with the Burgers equation. For this paper similar properties

TABLE 3.1
This table succinctly lists the requirements of the low-pass filters employed.

Properties	Mathematical expression
Normalized	$\int g = 1$
Nonnegative	$g(\mathbf{x}) > 0 \ \forall \mathbf{x}$
Decreasing	$\lvert\mathbf{x}_1\rvert \geq \lvert\mathbf{x}_2\rvert \Rightarrow g(\mathbf{x}_1) \leq g(\mathbf{x}_2)$
Even	$\lvert\mathbf{x}_1\rvert = \lvert\mathbf{x}_2\rvert \Rightarrow g(\mathbf{x}_1) = g(\mathbf{x}_2)$

are assumed for the filters. However, only sections 4, 5, and 6 deal with a general filter. All other sections deal exclusively with the Helmholtz filter, which also possesses all these characteristics. The Helmholtz filter is defined as

$$u = \bar{u} - \alpha^2 \bar{u}_{xx}, \tag{3.1}$$

and thus has an averaging kernel of

$$g^\alpha(x) = \frac{1}{2\alpha} \exp\left(-\frac{|x|}{\alpha}\right). \tag{3.2}$$

4. A general method. The successful regularization of the Burgers equations can be extended in several ways. As mentioned in the introduction, we had previously interpreted the convectively filtered Burgers (CFB) equations as an averaging of the characteristics [23]. Bhat, Fetecau, and Goodman interpreted the regularization of the Burgers equation as an averaging of the convective velocity, a Leray-type averaging [25]. Neither of these interpretations, when extended to the homentropic Euler equations, has led to the desired regularization of homentropic Euler equations. Here we examine yet another interpretation of the CFB equations, based on a conservation law perspective. This approach addresses the cascade of energy generated by the nonlinear terms. We then discuss how the technique used in regularizing the Burgers equation can be extended to a general technique to be used on conservation laws. Begin by looking at the inviscid Burgers equation

$$u_t + (uu)_x = 0. \tag{4.1}$$

The flux term represents that the quantity u is flowing into a control volume with velocity u. When the product rule is applied to the flux term the result is

$$u_t + uu_x + uu_x = 0. \tag{4.2}$$

Each nonlinear term in the above equation results in steepening waves which cascade energy into higher wave modes. It is this energy cascade that produces shocks. In section 2, it was discussed how this cascade of energy can be reduced by filtering the convective velocity. Thus the nondifferentiated term is passed through a low-pass filter. The resulting equation is

$$u_t + \bar{u}u_x + \bar{u}u_x = 0, \tag{4.3}$$

which has been referred to as the CFB equations. The portrayal of the CFB equations here differs from (1.1) and in previous papers [1, 3, 4, 2, 5, 6] by a factor of 2 but is identical under rescaling.

Now we extend this technique to a more general method. Suppose there is a single or multiple conservation laws of the form

$$Q_t + (Qu)_x = 0. \tag{4.4}$$

The proposed method is to apply the product rule to the nonlinear term and then apply a filter to the nondifferentiated quantities. This results in

$$Q_t + \bar{Q}u_x + \bar{u}Q_x = 0, \tag{4.5a}$$

$$\bar{u} = g * u, \tag{4.5b}$$

$$\bar{Q} = g * Q. \tag{4.5c}$$

We believe that this filtering of the nondifferentiated quantities will reduce the energy cascade and provide a regularization of the conservation law. This method can be shown to be a result of applying conservation principles using an "observable" divergence as shown in Mohseni [30]. As such, when this method is applied to the homentropic Euler and Euler equations, the new equations will be referred to as the observable homentropic Euler and the observable Euler equations.

5. Preservation of conserved quantities. Before we begin the examination of the observable homentropic Euler and observable Euler equations we will first examine how the modification of the nonlinear term still preserves the original conserved quantities. Consider (4.5). Integrate Q_t over the spatial domain and substitute equations (4.5b) and (4.5c) and the full definition of convolution to obtain

$$\frac{\partial}{\partial t}\int Q(x)\,dx = -\iint g(x-y)Q(y)u'(x)\,dy\,dx - \iint g(x-y)u(y)Q'(x)\,dy\,dx. \tag{5.1}$$

Integrate by parts to obtain

$$\frac{\partial}{\partial t}\int Q(x)\,dx = \iint g'(x-y)\left(Q(y)u(x) + u(y)Q(x)\right)dy\,dx. \tag{5.2}$$

If g is even, then g' is odd and $g'(x-y)$ is antisymmetric over $y = x$. Clearly $(Q(y)u(x) + u(y)Q(x))$ is symmetric over $y = x$, and thus by symmetry

$$\frac{\partial}{\partial t}\int Q(x)\,dx = 0. \tag{5.3}$$

From this it is determined the modified conservation law still conserves the original conserved quantity. Thus we see that the proposed method conserves the quantities that the original conservation laws were designed to preserve. This property is independent of the filter as long as it is even, which was a requirement of section 3.

6. Shock speed. Typically the speed of a shock in a conservation law is determined from the Rankine–Hugoniot jump conditions. However, for this case, equations (4.5) are not written in a conservative form, so applying the Rankine–Hugoniot jump conditions is not possible. However, using the definition of weak solution, we are able to determine the speed of a shock for equations (4.5) and show that it is similar if not identical to the speed of the unmodified conservation law.

First we establish notation used in this section and in later sections. The operator $[\cdot]$ will be used to quantify the difference between the right and left limits of a function

at a discontinuity. For example, if the limits of $u(x)$ at χ are defined as

$$\lim_{x\to\chi^+} u(x) = u_R, \tag{6.1}$$

$$\lim_{x\to\chi^-} u(x) = u_L, \tag{6.2}$$

then at χ

$$[u] = u_R - u_L. \tag{6.3}$$

The Rankine–Hugoniot jump conditions establish that for weak solutions of conservation laws of the form

$$\mathbf{v}_t + (\mathbf{f})_x = 0 \tag{6.4}$$

a traveling discontinuity must have a speed S, where S is defined as [31]

$$S = \frac{[\mathbf{f}]}{[\mathbf{v}]}. \tag{6.5}$$

Thus for the conservation law equation (4.4) the shock speed would be

$$S = \frac{[Qu]}{[Q]}. \tag{6.6}$$

We will now show that (4.5) will give a shock speed similar to that of the original equation, (4.4). Let Ω be a compact subset of $\mathbb{R}\times\mathbb{T}$. Let $\phi(x,t)$ be a continuously differentiable function that is compactly supported on Ω. For the functions Q and u to be a weak solution to (4.5a) they must satisfy

$$\iint_\Omega Q\phi_t + \bar{Q}u\phi_x + \bar{Q}_x u\phi + \bar{u}Q\phi_x + \bar{u}_x Q\phi \; dx\, dt = 0 \tag{6.7}$$

for all ϕ and all Ω. As a weak solution, when derivatives are properly defined, Q and u will satisfy (4.5a).

Assume that Q and u are continuously differentiable on Ω except at a single discontinuity located at $x=\chi(t)$. The line in Ω traced by $x=\chi(t)$ will be designated as Γ. We assume that Γ divides the domain Ω into two subdomains, Ω_l and Ω_r, signifying the left and right sections. Using (6.7) we will determine the speed of the shock, $S=\frac{\partial}{\partial t}\chi(t)$. Since $S=\frac{\partial}{\partial t}\chi(t)$, the vectors $n=\frac{\langle 1,-S\rangle}{\sqrt{1+S^2}}$ and $m=\frac{\langle -1,S\rangle}{\sqrt{1+S^2}}$ are normal to the line Γ in $\mathbb{R}\times\mathbb{T}$. The vector n points away from Ω_l, while vector m points away from Ω_r. We refer the reader to Figure 6.1 for a visual representation.

Apply the divergence theorem to the vector field $\langle \bar{Q}u\phi + \bar{u}Q\phi, Q\phi\rangle$ to establish

$$\iint_{\Omega_l} \left\langle \frac{\partial}{\partial x}, \frac{\partial}{\partial t}\right\rangle \cdot \langle \bar{Q}u\phi + \bar{u}Q\phi, Q\phi\rangle = \oint_{\partial\Omega_l} n\cdot \langle \bar{Q}u\phi + \bar{u}Q\phi, Q\phi\rangle. \tag{6.8}$$

Since ϕ is zero along the boundary of Ω_l except at Γ this can be reduced to

$$\iint_{\Omega_l} \bar{Q}_x u\phi + \bar{Q}u_x\phi + \bar{Q}u\phi_x + \bar{u}_x Q\phi + \bar{u}Q_x\phi + \bar{u}Q\phi_x + Q_t\phi + Q\phi_t = \int_\Gamma \frac{\bar{Q}u\phi + \bar{u}Q\phi}{\sqrt{1+S^2}} - \frac{SQ\phi}{\sqrt{1+S^2}}. \tag{6.9}$$

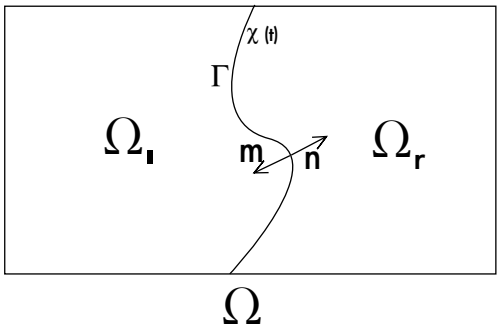

FIG. 6.1. *A diagram of the domain Ω, its subdomains Ω_l and Ω_r, and the curve Γ defined by $\chi(t)$. Also shown are the normal vectors to Γ.*

On the domain Ω_l, Q_x, Q_t, and u_x are well defined, and thus $\bar{Q}u_x\phi+\bar{u}Q_x\phi+Q_t\phi=0$. Thus it is established that

$$\iint_{\Omega_l} \bar{Q}_x u\phi + \bar{Q}u\phi_x + \bar{u}_x Q\phi + \bar{u}Q\phi_x + Q\phi_t = \int_\Gamma \frac{\bar{Q}u\phi + \bar{u}Q\phi}{\sqrt{1+S^2}} - \frac{SQ\phi}{\sqrt{1+S^2}}. \tag{6.10}$$

Similarly

$$\iint_{\Omega_r} \bar{Q}_x u\phi + \bar{Q}u\phi_x + \bar{u}_x Q\phi + \bar{u}Q\phi_x + Q\phi_t = \int_\Gamma -\frac{\bar{Q}u\phi + \bar{u}Q\phi}{\sqrt{1+S^2}} + \frac{SQ\phi}{\sqrt{1+S^2}}. \tag{6.11}$$

From the definition of a weak solution we know that

$$\iint_{\Omega_l+\Omega_r} \bar{Q}_x u\phi + \bar{Q}u\phi_x + \bar{u}_x Q\phi + \bar{u}Q\phi_x + Q\phi_t = 0 \tag{6.12}$$

and thus

$$\int_\Gamma -\frac{\bar{Q}u\phi + \bar{u}Q\phi}{\sqrt{1+S^2}} + \frac{SQ\phi}{\sqrt{1+S^2}} + \int_\Gamma \frac{\bar{Q}u\phi + \bar{u}Q\phi}{\sqrt{1+S^2}} - \frac{SQ\phi}{\sqrt{1+S^2}} = 0. \tag{6.13}$$

Note that the first term of (6.13) regards the values of Q and u on Ω_r, and the second term regards the values on Ω_l. Since this must hold on all Ω and all ϕ we establish

$$\lim_{x\to\chi^+} \left(-\bar{Q}u\phi - \bar{u}Q\phi + SQ\phi\right) + \lim_{x\to\chi^-} \left(\bar{Q}u\phi + \bar{u}Q\phi - SQ\phi\right) = 0, \tag{6.14}$$

which determines the shock speed to be

$$S = \frac{[\bar{Q}u + \bar{u}Q]}{[Q]}. \tag{6.15}$$

In section 3, our filter $g(x)$ was chosen to be even. Here another consequence of this choice is seen. For a filter satisfying conditions in section 3 and for small α one can find that

$$\bar{Q}(\chi) \approx \frac{Q_r + Q_l}{2}, \tag{6.16}$$

where Q_r and Q_l are the right and left limits of $Q(x)$ as $x \to \chi$. With this substitution we find that

$$S \approx \frac{[Qu]}{[Q]}. \tag{6.17}$$

Thus we see that the general technique will approximate the shock speed of the original conservation law. For the case where Q and u are constant to the left and right of the shock, the shock speeds of the original and modified conservation laws exactly match.

7. The one-dimensional homentropic Euler equations. Examine the homentropic Euler equations

$$\rho_t + (\rho u)_x = 0, \tag{7.1a}$$

$$(\rho u)_t + (\rho u u + P)_x = 0, \tag{7.1b}$$

with pressure defined as $P = \rho^\gamma$. Equations (7.1a) and (7.1b) are the mathematical expressions of conservation of mass and momentum, respectively. The homentropic Euler equations make the assumption that the entropy is constant throughout the entire domain, and thus the pressure can be expressed solely as a function of the density [31]. This differs from the isentropic Euler equations, where the entropy is constant along streamlines but not necessarily constant on the whole domain. It is found that the homentropic Euler equations are an accurate predictor of gas dynamics behavior for low pressure.

Both equations have a nonlinear term that fits the general method from section 4. Apply the method, break the nonlinear term apart, and then apply the filter to the nondifferentiated terms in the nonlinear terms to obtain the equations

$$\rho_t + \bar{\rho} u_x + \bar{u} \rho_x = 0, \tag{7.2a}$$

$$(\rho u)_t + (\overline{\rho u}) u_x + \bar{u} (\rho u)_x + P_x = 0, \tag{7.2b}$$

with pressure defined as $P = \rho^\gamma$. These equations are now referred to as the observable homentropic Euler equations. For the following analysis, the only filter that is considered is the Helmholtz filter (3.1).

7.1. Conservation of mass and momentum. The homentropic Euler equations (7.1) are conservation laws for mass and momentum. These equations are reflections of important physical principles. In order to be physically relevant it is desirable that any modification of the homentropic Euler equations should also preserve this structure. In section 5, we established that the technique used will preserve the conservative structure of the original equations. Here we reverify that result for the observable homentropic Euler equations (7.2) by casting the equations into a conservative form using the Helmholtz filter.

Using the definition of the Helmholtz filter (3.1) we get the following expressions for the unfiltered quantities:

$$u = \bar{u} - \alpha^2 \bar{u}_{xx}, \tag{7.3a}$$

$$\rho = \bar{\rho} - \alpha^2 \bar{\rho}_{xx}, \tag{7.3b}$$

$$\rho u = \overline{\rho u} - \alpha^2 (\overline{\rho u})_{xx}. \tag{7.3c}$$

By substituting (7.3a), (7.3b), and (7.3c) into equations (7.2) and then regrouping the similar terms, the observable homentropic Euler equations can be rewritten as

$$\rho_t + \left(\bar{\rho}\bar{u} - \alpha^2(\bar{u}\bar{\rho}_{xx} + \bar{\rho}\bar{u}_{xx}) + \alpha^2\bar{u}_x\bar{\rho}_x\right)_x = 0, \tag{7.4a}$$

$$(\rho u)_t + \left(\overline{\rho u}\bar{u} - \alpha^2(\bar{u}(\overline{\rho u})_{xx} + \overline{\rho u}\bar{u}_{xx}) + \alpha^2\bar{u}_x(\overline{\rho u})_x + P\right)_x = 0. \tag{7.4b}$$

This shows that the observable homentropic Euler equations can be written in a conservative form and preserve both mass, $\int \rho$, and momentum, $\int \rho u$, as well as the averaged mass, $\int \bar{\rho}$, and averaged momentum, $\int \overline{\rho u}$. Examination of equations (7.4) could lead to more geometric structure. It may also lead to the application of numerical techniques designed specifically for conservation laws.

7.2. Traveling wave solution. In this section, we establish that a previously known traveling wave solution to the homentropic Euler equations is, in fact, a traveling wave solution to the observable homentropic Euler equations. The traveling wave solution that we examine for the homentropic Euler equations is a single traveling shock.

Using the Rankine–Hugoniot jump conditions it is easy to establish that the following is a weak solution to the homentropic Euler equations (7.1):

$$u = \begin{cases} u_L, & x < St, \\ u_R, & x \geq St, \end{cases} \tag{7.5a}$$

$$\rho = \begin{cases} \rho_L, & x < St, \\ \rho_R, & x \geq St. \end{cases} \tag{7.5b}$$

The speed of the shock S is twice defined, once for each conservation law, by the Rankine–Hugoniot jump conditions as

$$S = \frac{[\rho u]}{[\rho]} \tag{7.6}$$

and

$$S = \frac{[\rho u u + P]}{[\rho u]}. \tag{7.7}$$

Thus u_L, u_R, ρ_L, and ρ_R must satisfy the relationship

$$\frac{[\rho u]}{[\rho]} = S = \frac{[\rho u u + P]}{[\rho u]}. \tag{7.8}$$

Using the results from section 6, it is not difficult to established that a weak solution to the observable homentropic Euler equations (7.2) will have a shock speed dictated by

$$S = \frac{[\bar{u}\rho + \bar{\rho}u]}{[\rho]}, \tag{7.9a}$$

$$S = \frac{[\bar{u}\rho u + \overline{\rho u}u + P]}{[\rho u]}. \tag{7.9b}$$

Next we will establish that (7.5) is also a weak solution to the observable homentropic Euler equations (7.4). It is straightforward to establish that with u defined as

in (7.5) and using the Helmholtz kernel definition (3.2) that $\bar{u}$ and $\bar{\rho}$ are

$$\bar{u} = \begin{cases} \frac{u_R - u_L}{2} \exp(\frac{x - St}{\alpha}) + u_L, & x < St, \\ \frac{u_L - u_R}{2} \exp(-\frac{x - St}{\alpha}) + u_R, & x \geq St, \end{cases} \tag{7.10}$$

$$\bar{\rho} = \begin{cases} \frac{\rho_R - \rho_L}{2} \exp(\frac{x - St}{\alpha}) + \rho_L, & x < St, \\ \frac{\rho_L - \rho_R}{2} \exp(-\frac{x - St}{\alpha}) + \rho_R, & x \geq St. \end{cases} \tag{7.11}$$

Thus the values of $\bar{u}$ and $\bar{\rho}$ at the position of the shock, $x = St$, are

$$\bar{u}(St, t) = \frac{u_R + u_L}{2}, \tag{7.12}$$

$$\bar{\rho}(St, t) = \frac{\rho_R + \rho_L}{2}. \tag{7.13}$$

Now, by using (7.12) and (7.13) and the definition of $[\cdot]$ one can re-express (7.9a) as

$$S = \frac{\frac{1}{2}(u_R + u_L)(\rho_R - \rho_L) + \frac{1}{2}(\rho_R + \rho_L)(u_R - u_L)}{[\rho]} \tag{7.14}$$

$$= \frac{(\rho_R u_R - \rho_L u_L)}{[\rho]} \tag{7.15}$$

$$= \frac{[\rho u]}{[\rho]}, \tag{7.16}$$

which is identical to (7.6). Similarly (7.9b) reduces to (7.7). Thus for a single traveling shock, the Rankine–Hugoniot jump conditions are identical for the homentropic Euler equations and the observable homentropic Euler equations. This validates our claim that (7.5) is a traveling weak solution for the observable homentropic Euler equations.

7.3. Shock thickness. With (7.5) validated as a traveling weak solution for the observable homentropic Euler equations, we establish an analytical result about shock thickness. Here the thickness of the shock is defined to be the length over which 90% of the amplitude change takes place, centered at the point of inflection.

The thickness of the shock in the traveling wave solution (7.5) will then be $2\alpha b$, where b is the value where

$$\int_{-b}^{b} \frac{1}{2} \exp(-|x|)\, dx = \int_{-\alpha b}^{\alpha b} \frac{1}{2\alpha} \exp\left(\frac{-|x|}{\alpha}\right) dx = 0.9. \tag{7.17}$$

The value b is a constant that is approximately $b \approx 2.30259$. The thickness of the shock, $2\alpha b$, is independent of ρ_R, ρ_L, u_R, and u_L. As such, the thickness of the shock varies linearly on the parameter α.

7.4. Diagonalization and eigenvalues. The homentropic Euler equations have very clearly defined eigenvalues, $u \pm a$, where $a^2 = \gamma \rho^{\gamma - 1}$ is the speed of sound. We have calculated how the averaging technique has affected the eigenvalues. An α-regularization can fundamentally change some of the original properties of the equations, such as in Bardos, Linshiz, and Titi [18], where the α-regularization of the two-dimensional incompressible Euler equations changed the ill-posedness of the Birkhoff–Rott equations. Thus we examine the changes to the eigenvalues of the equations to gain important information regarding the characteristic nature of the equations. If the averaging technique significantly changes the way that the characteristics

of the Euler equations behave, then there is little hope that there will be convergence to the entropy solution, as we have demonstrated in our previous work [23]. Additionally the eigenvalues, or the speed of the characteristics, are important in their use in establishing stability in numerical simulations. However, within this paper, these results have not been theoretically applied, and as such these calculations are presented in Appendix A.

7.5. Convergence to a weak solution. It is the goal of our technique to develop new equations that effectively capture the low wave mode (larger scale) behavior of the original equations. Thus it is desirable that the observable homentropic Euler equations approximate the homentropic Euler equations well. Ideally we can show that as the amount of filtering decreases, we regain the original equations. One crucial step in determining this is proving that as $\alpha \to 0$, the solutions to the observable homentropic Euler equations converge to a weak solution of the homentropic Euler equations. This, among other things, proves that as $\alpha \to 0$, the shocks produced by the observable homentropic Euler equations travel at the same speed as those of the homentropic Euler equations, which is desirable.

In order to properly show convergence to a weak solution, one must first establish the existence of solutions and then the compactness of those solutions, in order to establish a converging subsequence of solutions. As of yet, we have not been able to extend our existence theorems of the regularized Burgers equations (1.1) to the observable homentropic Euler equations (7.2). Without the existence theorem we have been unable to establish the a priori bounds needed to guarantee compactness. Until this can be accomplished, we operate under the assumption that solutions exist and have a converging subsequence. Thus far, all numerical simulations have given the impression that these assumptions are reasonable; however, proving such results can be found to be nontrivial. We assume that for every $\alpha > 0$ there exists a solution to equations (7.2) and that a subsequence of these solutions converges in L^1_{loc}. Furthermore, we assume that the solutions are bounded independent of α. The following summarizes these assumptions:

$$||u||_\infty < U, \tag{7.18a}$$

$$||\rho||_\infty < R, \tag{7.18b}$$

$$\lim_{\alpha \to 0} u = \tilde{u} \text{ in } L^1_{loc}, \tag{7.18c}$$

$$\lim_{\alpha \to 0} \rho = \tilde{\rho} \text{ in } L^1_{loc}. \tag{7.18d}$$

With these assumptions we are able to prove that the solutions to the observable homentropic Euler equations (7.2) will converge to weak solutions of the homentropic Euler equations (7.1). The examination of the claim is done with the Helmholtz filter, using both definitions (3.1) and (3.2). The following bounds are easily established by examining the kernel:

$$||g^\alpha||_1 = 1$$

and

$$\left|\left|\frac{\partial}{\partial x} g^\alpha\right|\right|_1 = \frac{1}{\alpha}.$$

These bounds, combined with Young's inequality [32] and the assumptions (7.18),

give the estimates

$$||\bar{u}||_\infty < U, \tag{7.19}$$

$$||\bar{\rho}||_\infty < R, \tag{7.20}$$

$$||\overline{\rho u}||_\infty < UR, \tag{7.21}$$

$$||\bar{u}_x||_\infty < \frac{1}{\alpha}U, \tag{7.22}$$

$$||\bar{\rho}_x||_\infty < \frac{1}{\alpha}R, \tag{7.23}$$

$$||(\overline{\rho u})_x||_\infty < \frac{1}{\alpha}UR. \tag{7.24}$$

Along with these estimates, the last piece needed is taken from Duoandikoetxea [33]. The following lemma is a restatement of Duoandikoetxea's Theorem 2.1 [33, p. 25].

LEMMA 7.1. *Let g be an integrable function on $\mathbb{R}$ such that $\int g = 1$. Define $g^\alpha = \frac{1}{\alpha}g(\frac{x}{\alpha})$. Then*

$$\lim_{\alpha\to 0} ||g^\alpha * f - f||_p = 0$$

if $f \in L^p$, $1 \le p < \infty$, and uniformly (i.e., when $p = \infty$) if $f \in C_0(\mathbb{R})$.

With Lemma 7.1 the convergence to weak solutions can now be proven.

Begin by multiplying equations (7.4) by a test function ϕ and integrate over time and space. It is assumed that ϕ has an infinite number of bounded and continuous derivatives and is compactly supported. Doing this we obtain the equations

$$\int_{\mathbb{R}}\int_0^T \rho_t\phi + \left(\bar{\rho}\bar{u} - \alpha^2(\bar{u}\bar{\rho}_{xx} + \bar{\rho}\bar{u}_{xx}) + \alpha^2\bar{u}_x\bar{\rho}_x\right)_x \phi\, dt\, dx = 0, \tag{7.25a}$$

$$\int_{\mathbb{R}}\int_0^T (\rho u)_t\phi + \left(\left(\overline{\rho u}\bar{u} - \alpha^2(\bar{u}(\overline{\rho u})_{xx} + \overline{\rho u}\bar{u}_{xx}) + \alpha^2\bar{u}_x(\overline{\rho u})_x\right) + P\right)_x \phi\, dt\, dx = 0. \tag{7.25b}$$

Integrate by parts to obtain

$$\int_{\mathbb{R}}\int_0^T \rho\phi_t + (\bar{\rho}\bar{u})\,\phi_x\, dt\, dx = \int_{\mathbb{R}}\int_0^T \left(\alpha^2(\bar{u}\bar{\rho}_{xx} + \bar{\rho}\bar{u}_{xx}) - \alpha^2\bar{u}_x\bar{\rho}_x\right)\phi_x\, dt\, dx, \tag{7.26a}$$

$$\int_{\mathbb{R}}\int_0^T (\rho u)\phi_t + (\overline{\rho u}\bar{u} + P)\,\phi_x\, dt\, dx = \int_{\mathbb{R}}\int_0^T \left(\alpha^2(\bar{u}(\overline{\rho u})_{xx} + \overline{\rho u}\bar{u}_{xx}) - \alpha^2\bar{u}_x(\overline{\rho u})_x\right)\phi_x\, dt\, dx. \tag{7.26b}$$

Clearly if the right-hand sides of (7.26a) and (7.26b) limit to zero, then the limit of ρ and u is a weak solution to the homentropic Euler equations. Begin by examining the term

$$\int_{\mathbb{R}}\int_0^T \alpha^2\bar{u}\bar{\rho}_{xx}\phi_x\, dt\, dx. \tag{7.27}$$

Substitute the definition of the averaging so that $\alpha^2\bar{\rho}_{xx} = \bar{\rho} - \rho$ and examine the quantity

$$\int_{\mathbb{R}}\int_0^T \bar{u}(\bar{\rho} - \rho)\phi_x\, dt\, dx. \tag{7.28}$$

It was established that $\bar{u}$ and ϕ_x are bounded, and by Lemma 7.1 $(\bar{\rho} - \rho)$ converges in L^1 to zero. Thus we find

$$\lim_{\alpha \to 0} \int_{\mathbb{R}} \int_0^T \alpha^2 \bar{u} \bar{\rho}_{xx} \phi_x \, dt \, dx = \int_{\mathbb{R}} \int_0^T \bar{u}(\bar{\rho} - \rho) \phi_x \, dt \, dx = 0, \tag{7.29}$$

and the similar terms can be treated likewise.

Next examine the term

$$\int_{\mathbb{R}} \int_0^T \alpha^2 \bar{u}_x (\overline{\rho u})_x \phi_x \, dt \, dx. \tag{7.30}$$

Perform an integration by parts to obtain

$$-\int_{\mathbb{R}} \int_0^T \alpha^2 \bar{u} (\overline{\rho u})_{xx} \phi_x \, dt \, dx - \int_{\mathbb{R}} \int_0^T \alpha^2 \bar{u} (\overline{\rho u})_x \phi_{xx} \, dt \, dx. \tag{7.31}$$

The first term in (7.31) limits to zero from the steps shown above. The second term can be bounded with the estimates found from Young's inequality,

$$\left\| \int_{\mathbb{R}} \int_0^T \alpha^2 \bar{u} (\overline{\rho u})_x \phi_{xx} \, dt \, dx \right\| \leq \int_{\mathbb{R}} \int_0^T \alpha^2 U \frac{1}{\alpha} U R |\phi_{xx}| \, dt \, dx \tag{7.32}$$

$$= \alpha U^2 R ||\phi_{xx}||_1, \tag{7.33}$$

and thus limits to zero. The similar terms can be treated likewise. Thus we see that solutions to equations (7.4) converge to weak solutions of the homentropic Euler equations as $\alpha \to 0$.

7.6. Numerics. In this section, we discuss the numerical techniques we used to simulate the observable homentropic Euler equations and the homentropic Euler equations. As we discussed in the introduction, we are proposing an inviscid regularization of the Euler equations. As such we wish to avoid any numerical dissipation or artificial viscosity from our numerical method, as this numerical dissipation could lead to a false sense of regularization. We also wish to isolate our regularization technique from any complexities, such as boundary conditions, so we use periodic boundary conditions. Thus we choose a pseudospectral method, as this is known to prevent numerical viscosity to the extent possible [34] and forces periodic boundary conditions.

For the homentropic Euler equations, shocks are expected to form in the simulations. If a pseudospectral method were used, the Gibbs phenomenon would cause spurious oscillations; thus we use a well-established numerical method, utilized as described in section 7.6.2.

7.6.1. Numerical simulations of the observable homentropic Euler equations. In practical applications, it is the mean quantity that is desired, since any physical measurement is in effect an averaged quantity. In turbulence simulations (LES and LANS-α) and other averaging techniques that address shock behavior, only the evolution of the averaged quantities is conducted [35, 36, 6, 37, 2]. In doing so, the numerical resolution required for accurate simulations is lessened. It is our hope that the averaging technique that we present here will be used in turbulence and shock simulation. In that regard, for the observable homentropic Euler equations we wish only to resolve the averaged quantities in our numerical simulations. To obtain the

evolution equations of the averaged quantities, we first apply the Helmholtz filter to equations (7.2) and add $(\bar{\rho}\bar{u})_x$ or $(\overline{\rho u}\bar{u})_x$ to both sides:

$$\bar{\rho}_t + (\bar{\rho}\bar{u})_x = (\bar{\rho}\bar{u})_x - \overline{(\bar{\rho}u_x + \bar{u}\rho_x)}, \tag{7.34a}$$

$$\overline{\rho u}_t + \left(\overline{\rho u}\bar{u} + \bar{P}\right)_x = (\overline{\rho u}\bar{u})_x - \overline{(\overline{\rho u}u_x + \bar{u}(\rho u)_x)}. \tag{7.34b}$$

Then we use the definition of the Helmholtz filter (3.1) to manipulate the equations to

$$\bar{\rho}_t + (\bar{\rho}\bar{u})_x = \overline{(1-\alpha^2\partial_x^2)\,(\bar{\rho}\bar{u})_x - \bar{\rho}(\bar{u}_x - \alpha^2\bar{u}_{xxx}) - \bar{u}(\bar{\rho}_x - \alpha^2\bar{\rho}_{xxx})}, \tag{7.35a}$$

$$\overline{\rho u}_t + \left(\overline{\rho u}\bar{u} + \bar{P}\right)_x = \overline{(1-\alpha^2\partial_x^2)\,(\overline{\rho u}\bar{u})_x - \overline{\rho u}(\bar{u}_x - \alpha^2\bar{u}_{xxx}) - \bar{u}((\overline{\rho u})_x - \alpha^2(\overline{\rho u})_{xxx})}. \tag{7.35b}$$

One can then simplify to obtain

$$\bar{\rho}_t + (\bar{\rho}\bar{u})_x = -3\alpha^2\overline{(\bar{u}_x\bar{\rho}_x)_x}, \tag{7.36a}$$

$$\overline{\rho u}_t + \left(\overline{\rho u}\bar{u} + \bar{P}\right)_x = -3\alpha^2\overline{(\bar{u}_x(\overline{\rho u})_x)_x}. \tag{7.36b}$$

The equations are now completely in terms of the averaged quantities, with the right-hand sides being the potentially regularizing terms.

In order to reduce the potential for numerical dissipation we use a pseudospectral method to solve equations (7.36). We advance the equations in time with an explicit Runge–Kutta–Fehlberg predictor/corrector (RK45) [6]. The initial time step is chosen small enough to achieve stability and is then varied by the code using the formula

$$h_{i+1} = \gamma h_i \left(\frac{\varepsilon h_i}{||\bar{\rho}_i - \hat{\rho}_i||_2}\right)^{\frac{1}{4}}. \tag{7.37}$$

Thus the new time step is chosen from the previous time step and the amount of error between the predicted density, $\bar{\rho}$, and the corrected density, $\hat{\rho}$. The relative error tolerance was chosen at $\varepsilon = 10^{-4}$ and the safety factor $\gamma = 0.9$. If the new time step chosen was found to violate the CFL condition, the time step was chosen according to the velocity speed and the speed of sound with CFL number 0.5.

Spatial derivatives and the inversion of the Helmholtz operator were computed in the Fourier domain. The terms were converted into the Fourier domain using a fast Fourier transform, multiplied by the appropriate term, and then converted back into the physical domain.

A number of high resolution simulations were done at the resolution of $2^{14} = 65536$ grid points on the domain $[0, 2\pi]$. We found that some long-term simulations may suffer from long-term numerical instabilities. In order to control this long-term instability, every 200 time steps we zero out all the wave modes with a wave number higher than $\frac{N}{3}$, where N is the highest Fourier wave mode simulated. Wave modes higher than $\frac{2N}{3}$ are set to zero at every nonlinear multiplication to prevent aliasing. Numerical runs were conducted for values $\alpha = 0.10, 0.09, \ldots, 0.02, 0.01$. In the worst-case scenario, $\alpha = 0.01$, the wave modes that are zeroed are over an order of magnitude higher than $\frac{1}{\alpha}$, as seen in Figure 7.1.

We attribute this error to the right-hand side of equations (7.36) for the following reasons. Examine the term

$$-3\alpha^2\overline{(\bar{u}_x\bar{\rho}_x)_x}. \tag{7.38}$$

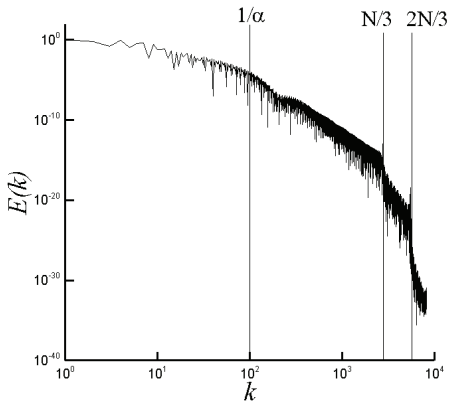

FIG. 7.1. *The spectral energy of u. The vertical lines represent three significant wave numbers. From left to right the lines represent* $\frac{1}{\alpha}$, $\frac{N}{3}$, *and* $\frac{2N}{3}$, *where N is the highest Fourier wave mode simulated. The wave mode* $\frac{N}{3}$ *is the highest wave mode that is ever zeroed out in the simulations. Here with* $\alpha = 0.01$ *you can see that zeroing of wave modes takes place an order of magnitude higher than where the filtering has its effect. This graph was taken from simulations of example problem* (7.42). *Here* $t = 0.1$, $N = 2^{13}$, *and* $n = 2^{14}$, *where N is the number of Fourier modes resolved and n is the number of grid points.*

Expand the term to

$$-3\alpha^2\overline{\bar{u}_{xx}\bar{\rho}_x + \bar{u}_x\bar{\rho}_{xx}} \tag{7.39}$$

and specifically notice the $\bar{u}_x\bar{\rho}_{xx}$ term. This term can be considered as a viscosity-like term that changes signs with $\bar{u}_x$. Now along the expansion wave $\bar{u}_x > 0$, and thus there is a negative second derivative or viscosity-like term. Negative viscosity is inherently unstable, so we attribute the numerical instabilities to this. This could be compared to the backscatter of energy to larger scales that is observed in turbulence.

7.6.2. Numerics for the homentropic Euler equations. For the numerical simulations of the homentropic Euler equations there are many established, available techniques [31]. We chose to use the Richtmyer method, a well-established and low-order method, as described by [31]. This method is a second-order, finite-difference scheme and employs an artificial viscosity. This method requires an artificial viscosity for stability when examining the Riemann problem. Several different values of ν were tested to see that the value did not significantly affect the solutions on the time interval examined. For the numerical simulations shown here, the artificial viscosity was set at $\nu = 0.08$. For reference, the simulations were done with 2^{14} grid points on a $[0, 2\pi]$ domain.

7.7. Numerical results. This section examines some numerical simulations performed on equations (7.36) with the technique described in the previous section. A shock tube or Riemann problem exhibits both shocks and expansion waves, some of the key behaviors of the homentropic Euler equations. Our pseudospectral method enforces periodic boundary conditions, so we created two pressure jumps in the initial conditions resolving this issue. Thus essentially a double shock tube problem is considered where there are two discontinuities in the initial conditions to make the left- and right-hand side boundary conditions identical. The example problem considered

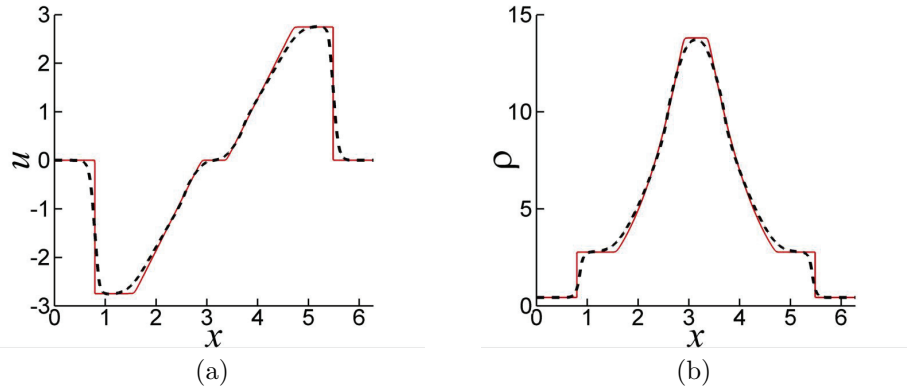

(a) (b)

FIG. 7.2. *A numerical simulation of the observable homentropic Euler equations (dashed line) plotted against the solution to the homentropic Euler equations (solid line). Here* $\alpha = 0.05$. *In both figures, it is clear that the observable homentropic Euler equations are capturing both the expansion wave and shock behavior.* (a) *The velocity.* (b) *The density.*

is

$$u_0(x) = 0, \tag{7.40}$$

$$a_0(x) = \begin{cases} 1, & 0 < x \leq \frac{2\pi}{3}, \\ 2, & \frac{2\pi}{3} < x \leq \frac{4\pi}{3}, \\ 1, & \frac{4\pi}{3} < x \leq 2\pi, \end{cases} \tag{7.41}$$

which for $\gamma = 1.4$, the constant for air, is equivalent to

$$u_0(x) = 0, \tag{7.42}$$

$$\rho_0(x) = \begin{cases} 0.43120, & 0 < x \leq \frac{2\pi}{3}, \\ 13.7984, & \frac{2\pi}{3} < x \leq \frac{4\pi}{3}, \\ 0.43120, & \frac{4\pi}{3} < x \leq 2\pi. \end{cases} \tag{7.43}$$

In our previous work, we established that for the CFB equations (1.1) initial conditions with discontinuities were excluded in order to avoid nonentropic behavior [5]. By averaging the initial conditions it was proven that the solution to the CFB equations would be regularized for all time. This was done by averaging the initial conditions with the same filter used on the velocity. We use this same approach here. Thus when the filter is applied to the entire system to obtain equations (7.36), the initial conditions are filtered twice, with the same filter used on the equations.

In the simulation of the double shock tube problem the observable homentropic Euler equations are displaying behavior similar to that of the homentropic Euler equations. Figures 7.2 and 7.3 show the solutions to the two sets of equations imposed on each other. One can see that the solutions to the observable homentropic Euler equations capture both the expansion wave and the shock front. The solutions to the observable homentropic Euler equations are seen to be smooth, with the solutions tightening to the solutions of the homentropic Euler equations as α decreases.

Now we check the convergence of the solutions of the observable homentropic Euler equations to the solution of the homentropic Euler equations as $\alpha \to 0$. Figures 7.4 and 7.5 show that as $\alpha \to 0$ the error in the L^1 norm appears to be approaching zero

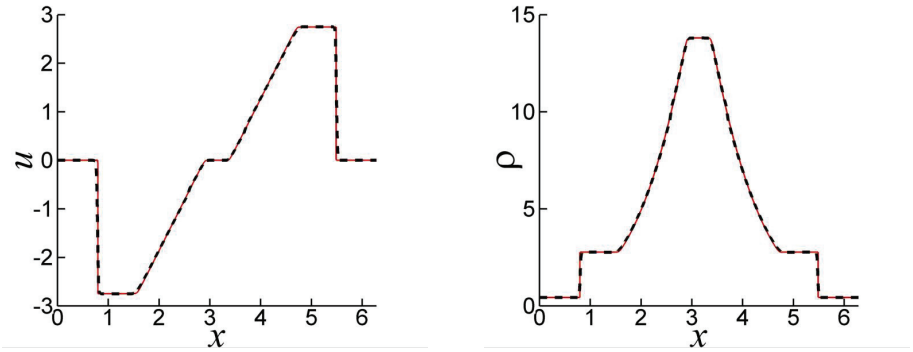

(a) (b)

FIG. 7.3. *A numerical simulation of the observable homentropic Euler equations (dashed line) plotted against the solution to the homentropic Euler equations (solid line). Here* $\alpha = 0.01$. *In both figures, it is clear that the observable homentropic Euler equations are capturing both the expansion wave and shock behavior. With the lower value of* α *the fit is much closer.* (a) *The velocity.* (b) *The density.*

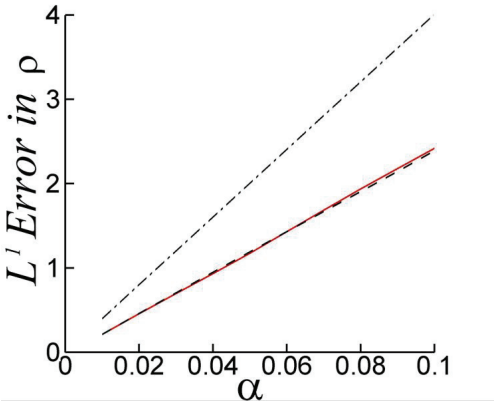

FIG. 7.4. *The difference between the density in solutions of the observable homentropic Euler equations and the solution of the homentropic Euler equations in the* L^1 *norm as* $\alpha \to 0$. *As* $\alpha \to 0$ *the difference in the solutions also approaches zero. The measurements were taken for* $\alpha = 0.01, 0.02, \ldots, 0.1$ *at times* $t = 0$ *(dashed dotted line),* $t = 0.2$ *(solid line), and* $t = 0.4$ *(dashed line).*

for the example problem. This suggests that the solutions of the observable homentropic Euler equations converge to the solutions of the homentropic Euler equations.

7.8. Kinetic energy rates. In addition to checking solution profiles, we examine the effect that our averaging technique has upon the kinetic energy. For the homentropic Euler equations we define kinetic energy as $\frac{1}{2}\rho u^2$. For the observable homentropic Euler equations there are three different averaged quantities, $\bar{\rho}$, $\bar{u}$, and $\overline{\rho u}$. With these quantities, kinetic energy can be defined in a variety of ways. In this section we examine a kinetic energy with unfiltered terms, $\frac{1}{2}\rho u^2$, and a kinetic energy with filtered terms, $\frac{1}{2}\bar{\rho}\bar{u}^2$. We have also examined the possible kinetic energies $\frac{1}{2}\overline{\rho u}\bar{u}$ and $\frac{\overline{\rho u}^2}{2\bar{\rho}}$, but for the example that we are considering, the difference between them

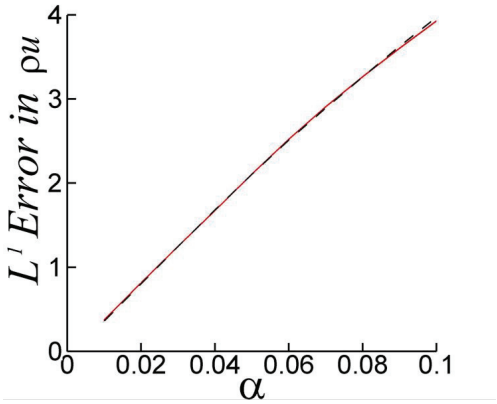

FIG. 7.5. *The difference between the momentum in solutions of the observable homentropic Euler equations and the solution of the homentropic Euler equations in the* L^1 *norm as* $\alpha \to 0$. *As* $\alpha \to 0$ *the difference in the solutions also approaches zero. The measurements were taken for* $\alpha = 0.01, 0.02, \ldots, 0.1$ *at times* $t = 0.2$ *(solid line) and* $t = 0.4$ *(dashed line).*

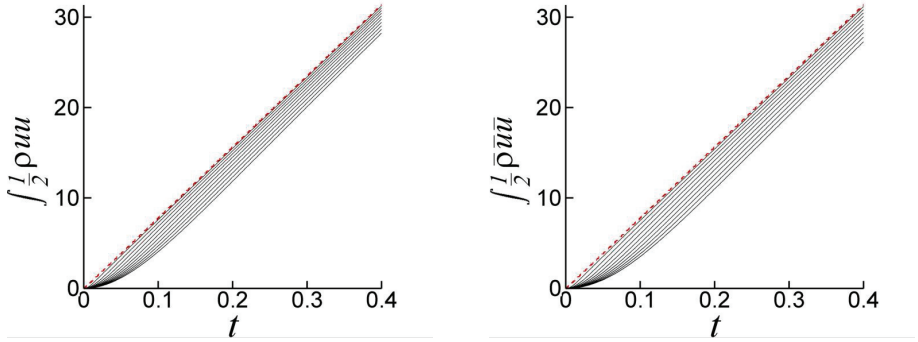

(a) (b)

FIG. 7.6. *The kinetic energy of the homentropic Euler equations and the observable homentropic Euler equations. The energy for the true solution of the homentropic Euler equations is shown as a dashed line. The simulations of the observable homentropic Euler equations for* $\alpha = 0.01, 0.02, \ldots, 0.1$ *are shown as solid lines. The bottommost line represents* $\alpha = 0.1$. *As* α *decreases the energy approaches the energy of the homentropic Euler equations.* (a) *Plots of the unfiltered kinetic energies,* $\frac{1}{2}\rho u^2$. (b) *Plots of the filtered kinetic energies,* $\frac{1}{2}\bar{\rho}\bar{u}^2$. *When examined, the plots of* $\frac{1}{2}\overline{\rho u}\bar{u}$ *and* $\frac{\overline{\rho u}^2}{2\bar{\rho}}$ *were identical to this one.*

and $\frac{1}{2}\bar{\rho}\bar{u}^2$ was of the order 10^{-14} and thus negligible. For flows with more small scale behavior, we would expect this difference to be more significant.

For the shock tube problem, the kinetic energy of the system clearly starts at zero. For the homentropic Euler equations the solution is self-similar, depending only on the variable $\frac{x}{t}$. Thus the kinetic energy for the homentropic Euler equations will be a linear function of time. This can be seen in Figure 7.6. We find that the energies of the observable homentropic Euler equations mimic that of the homentropic Euler equations. In the simulations of the observable homentropic Euler equations there is a brief period where the energy growth is curved before it appears to behave linearly.

We attribute this to the averaging of the initial conditions. As we would expect, as α decreases the energies grow closer to those of the homentropic Euler equations.

8. The one-dimensional Euler equations. While the homentropic Euler equations are good for low pressures, to have real impact we want our technique to be able to capture the behavior of the full one-dimensional Euler equations. With the observable homentropic Euler equations showing promise, we attempt to use the same general methodology on the one-dimensional Euler equations. The one-dimensional Euler equations consist of three conservation laws paired with a constitutive law. The conservation laws are conservation of mass, momentum, and energy. For the constitutive law, this paper is considering an ideal gas. Thus the one-dimensional Euler equations considered, in conservation form, are

$$\rho_t + (\rho u)_x = 0, \tag{8.1a}$$

$$(\rho u)_t + (\rho u u + P)_x = 0, \tag{8.1b}$$

$$(\rho e)_t + (\rho e u + u P)_x = 0, \tag{8.1c}$$

$$P = (\gamma - 1)\left(\rho e - \frac{1}{2}\rho u^2\right). \tag{8.1d}$$

The technique described in section 4 applies the product rule to nonlinear terms, and then the nondifferentiated quantities are spatially filtered. Again this is to reduce the production of higher wave modes as time progresses. When our averaging technique is applied, the new equations are

$$\rho_t + \bar{\rho} u_x + \bar{u}\rho_x = 0, \tag{8.2a}$$

$$(\rho u)_t + \overline{\rho u} u_x + \bar{u}(\rho u)_x + P_x = 0, \tag{8.2b}$$

$$(\rho e)_t + \overline{\rho e} u_x + \bar{u}(\rho e)_x + \overline{P} u_x + \bar{u} P_x = 0, \tag{8.2c}$$

$$P = (\gamma - 1)\left(\rho e - \frac{1}{2}\rho u^2\right), \tag{8.2d}$$

which we refer to as observable Euler equations. The general method established in section 4 does not address exactly how to handle the pressure terms. In the conservation of momentum equation (8.1b) the pressure term is left unaffected, as in the observable homentropic Euler equations. However, the $(uP)_x$ term in the conservation of energy equation (8.1c) is averaged using the general method. We have found in earlier numerical simulations that not performing the averaging technique on this term leads to some nonphysical behavior.

We now go on to show results for the observable Euler equations similar to those shown in section 7.

8.1. Conservation of mass and momentum. The Euler equations (8.1) are conservation laws that address conservation of mass, momentum, and energy. This section shows that the observable Euler equations preserve these same quantities by casting the equations into a conservative form. It would be sufficient to refer the reader back to sections 5 and 7.1 and note that our method does not disturb the conservation structure of the Euler equations. However, explicitly showing this for the observable Euler equations for the Helmholtz filter has merit, as it demonstrates a new form of the equations which are of interest.

When using the Helmholtz filter, the nonfiltered equations can be expressed by their filtered counterparts using (3.1). Using this filter, equations (8.2) can be rewrit-

ten as

$$\rho_t + \left[\bar{\rho}\bar{u} - \alpha^2(\bar{u}\bar{\rho}_{xx} + \bar{\rho}\bar{u}_{xx}) + \alpha^2\bar{u}_x\bar{\rho}_x\right]_x = 0, \tag{8.3a}$$

$$(\rho u)_t + \left[\overline{\rho u}\bar{u} - \alpha^2(\bar{u}(\overline{\rho u})_{xx} + \overline{\rho u}\bar{u}_{xx}) + \alpha^2\bar{u}_x(\overline{\rho u})_x + P\right]_x = 0, \tag{8.3b}$$

$$\begin{aligned}(\rho e)_t + \Big[&\overline{\rho e}\bar{u} - \alpha^2(\bar{u}(\overline{\rho e})_{xx} + \overline{\rho e}\bar{u}_{xx}) + \alpha^2\bar{u}_x(\overline{\rho e})_x \\ &+ \overline{P}\bar{u} - \alpha^2(\bar{u}\overline{P}_{xx} + \overline{P}\bar{u}_{xx}) + \alpha^2\bar{u}_x\overline{P}_x\Big]_x = 0.\end{aligned} \tag{8.3c}$$

In this conservation form it is easy to see that mass $\int \rho$, momentum $\int \rho u$, and energy $\int \rho e$ are conserved.

8.2. Traveling wave solution. In section 7.2 it was established that certain traveling shock solutions to the homentropic Euler equations are also solutions to the observable homentropic Euler equations. The section establishes a similar result for the Euler and observable Euler equations using the same techniques. Again the operator $[\cdot]$ is used as defined in section 6.

Again we examine a traveling shock of the form

$$\rho = \begin{cases} \rho_L, & x < St, \\ \rho_R, & x \geq St, \end{cases} \tag{8.4a}$$

$$\rho u = \begin{cases} M_L, & x < St, \\ M_R, & x \geq St, \end{cases} \tag{8.4b}$$

$$\rho e = \begin{cases} E_L, & x < St, \\ E_R, & x \geq St. \end{cases} \tag{8.4c}$$

Using the Rankine–Hugoniot jump conditions (6.5) we can establish that at a discontinuity a weak solution to the Euler equations (8.1) must satisfy

$$S = \frac{[\rho u]}{[\rho]}, \tag{8.5a}$$

$$S = \frac{[\rho u u + P]}{[\rho u]}, \tag{8.5b}$$

$$S = \frac{[\rho e u + u P]}{[\rho e]}. \tag{8.5c}$$

Using the results from sections 6 and 7.2 we can establish that a weak solution to the observable Euler equations (8.2) will have a shock speed dictated by

$$S = \frac{[\bar{\rho}u + \bar{u}\rho]}{[\rho]}, \tag{8.6a}$$

$$S = \frac{[\overline{\rho u}u + \bar{u}\rho u + P]}{[\rho u]}, \tag{8.6b}$$

$$S = \frac{[\overline{\rho e}u + \bar{u}\rho e + \overline{P}u + \bar{u}P]}{[\rho e]}. \tag{8.6c}$$

Using the exact same computations as in section 7.2 it is a straightforward process to show that for solutions of the form (8.4), the jump conditions for the Euler equations (8.5) are exactly equivalent to the jump conditions for the observable Euler equations (8.6). Thus (8.4) with values satisfying equations (8.5) will be traveling weak solutions to the observable Euler equations.

Additionally, using the same analysis found in section 7.3, it can again be shown that the thickness of the shocks for the traveling solution will decrease linearly with α.

8.3. Eigenvalues. Much like the homentropic Euler equations, the one-dimensional Euler equations have very well defined eigenvalues $u, u \pm a$. We again examine how the averaging technique has affected the eigenvalues of the system. As these calculations have not been directly applied in the scope of this paper, these calculations can be found in Appendix B.

8.4. Convergence to a weak solution. Section 7.5 showed that with certain assumptions made on the solutions of the observable Euler equations, the solutions converge to weak solutions of the homentropic Euler equations as $\alpha \to 0$. With similar assumptions on the observable Euler equations, we are able to prove that the solutions converge to weak solutions of the Euler equations.

With an existence and uniqueness proof for the observable Euler equations not yet developed, we are again forced to make several assumptions. We assume that for every $\alpha > 0$ there exists a solution to equations (8.2) and that a subsequence of these solutions converges in L^1_{loc}. Additionally, we assume that the solutions are bounded independent of α. Thus far, all numerical simulations have given the impression that these assumptions are reasonable; however, proving such results can be found to be nontrivial. The following summarizes these assumptions:

$$||u||_\infty < U, \tag{8.7a}$$

$$||\rho||_\infty < R, \tag{8.7b}$$

$$||e||_\infty < E, \tag{8.7c}$$

$$\lim_{\alpha\to 0} u = \tilde{u} \text{ in } L^1_{loc}, \tag{8.7d}$$

$$\lim_{\alpha\to 0} \rho = \tilde{\rho} \text{ in } L^1_{loc}, \tag{8.7e}$$

$$\lim_{\alpha\to 0} e = \tilde{e} \text{ in } L^1_{loc}. \tag{8.7f}$$

With these assumptions we are able to prove that the weak solutions to the observable Euler equations (8.2) will converge to weak solutions of the Euler equations (8.1) as $\alpha \to 0$. The examination of this claim is done with the Helmholtz filter, which has bounds already established in section 7.5. These bounds can be combined with Young's inequality [32] and assumptions (8.7) to obtain estimates on the filtered quantities. The following estimates essentially state that the filtered quantities have the same infinity bound as the unfiltered quantities and that the first derivatives of the filtered quantities are of order $\frac{1}{\alpha}$. Explicitly these estimates are

$$||\bar{u}||_\infty < U, \tag{8.8}$$

$$||\bar{\rho}||_\infty < R, \tag{8.9}$$

$$||\overline{\rho u}||_\infty < UR, \tag{8.10}$$

$$||\bar{e}||_\infty < E, \tag{8.11}$$

$$||\overline{\rho e}||_\infty < ER, \tag{8.12}$$

$$||\overline{P}||_\infty < (\gamma - 1)\left(ER + \frac{1}{2}RU^2\right), \tag{8.13}$$

$$||\bar{u}_x||_\infty < \frac{1}{\alpha}U, \tag{8.14}$$

$$||\bar{\rho}_x||_\infty < \frac{1}{\alpha}R, \tag{8.15}$$

$$||(\overline{\rho u})_x||_\infty < \frac{1}{\alpha}UR, \tag{8.16}$$

$$||(\overline{\rho e})_x||_\infty < \frac{1}{\alpha} ER, \tag{8.17}$$

$$||\overline{P}_x||_\infty < \frac{1}{\alpha}(\gamma - 1)\left(ER + \frac{1}{2}RU^2\right). \tag{8.18}$$

Begin by multiplying equations (8.3) by a test function ϕ and integrate over time and space. The test function ϕ has an infinite number of bounded and continuous derivatives and is compactly supported. After the multiplication and integration the equations become

$$\int_{\mathbb{R}}\int_0^T \rho_t\phi + \left(\bar{\rho}\bar{u} - \alpha^2(\bar{u}\bar{\rho}_{xx} + \bar{\rho}\bar{u}_{xx}) + \alpha^2\bar{u}_x\bar{\rho}_x\right)_x \phi\, dt\, dx = 0, \tag{8.19a}$$

$$\int_{\mathbb{R}}\int_0^T (\rho u)_t\phi + \left(\left(\overline{\rho u}\bar{u} - \alpha^2(\bar{u}(\overline{\rho u})_{xx} + \overline{\rho u}\bar{u}_{xx}) + \alpha^2\bar{u}_x(\overline{\rho u})_x\right) + P\right)_x \phi\, dt\, dx = 0, \tag{8.19b}$$

$$\begin{aligned}\int_{\mathbb{R}}\int_0^T (\rho e)_t\phi + \Big[&\overline{\rho e}\bar{u} - \alpha^2(\bar{u}(\overline{\rho e})_{xx} + \overline{\rho e}\bar{u}_{xx}) + \alpha^2\bar{u}_x(\overline{\rho e})_x \\ &+ \overline{P}\bar{u} - \alpha^2(\bar{u}\overline{P}_{xx} + \overline{P}\bar{u}_{xx}) + \alpha^2\bar{u}_x\overline{P}_x\Big]_x \phi\, dt\, dx = 0.\end{aligned} \tag{8.19c}$$

Integrate by parts to obtain

$$\int_{\mathbb{R}}\int_0^T \rho\phi_t + (\bar{\rho}\bar{u})\,\phi_x\, dt\, dx = \int_{\mathbb{R}}\int_0^T \left(\alpha^2(\bar{u}\bar{\rho}_{xx} + \bar{\rho}\bar{u}_{xx}) - \alpha^2\bar{u}_x\bar{\rho}_x\right)\phi_x\, dt\, dx, \tag{8.20a}$$

$$\int_{\mathbb{R}}\int_0^T (\rho u)\phi_t + (\overline{\rho u}\bar{u} + P)\,\phi_x\, dt\, dx = \int_{\mathbb{R}}\int_0^T \left(\alpha^2(\bar{u}(\overline{\rho u})_{xx} + \overline{\rho u}\bar{u}_{xx}) - \alpha^2\bar{u}_x(\overline{\rho u})_x\right)\phi_x\, dt\, dx, \tag{8.20b}$$

$$\begin{aligned}\int_{\mathbb{R}}\int_0^T (\rho e)\phi_t + \left(\overline{\rho e}\bar{u} + \overline{P}\bar{u}\right)\phi_x\, dt\, dx = &\int_{\mathbb{R}}\int_0^T \left(\alpha^2(\bar{u}(\overline{\rho e})_{xx} + \overline{\rho e}\bar{u}_{xx}) - \alpha^2\bar{u}_x(\overline{\rho e})_x\right)\phi_x\, dt\, dx \\ &+ \int_{\mathbb{R}}\int_0^T \left(\alpha^2(\bar{u}\overline{P}_{xx} + \overline{P}\bar{u}_{xx}) - \alpha^2\bar{u}_x\overline{P}_x\right)\phi_x\, dt\, dx.\end{aligned} \tag{8.20c}$$

Clearly if the right-hand side of the above equations limits to 0 as $\alpha \to 0$, then convergence to a weak solution is proven. Since the calculations are all but identical, the reader is referred to section 7.5 to prove that the right-hand sides of the equations do limit to 0. With the right-hand side limiting to 0 we find that ρ, u, and e are, in fact, limiting to a weak solution of the Euler equations.

8.5. Numerics. The numerical simulations for the observable Euler equations are the same as those discussed in section 7.6 with the addition of the energy equation. The equations simulated here are

$$\bar{\rho}_t + (\bar{\rho}\bar{u})_x = -3\alpha^2\overline{(\bar{u}_x\bar{\rho}_x)_x}, \tag{8.21a}$$

$$\overline{\rho u}_t + \left(\overline{\rho u}\bar{u} + \bar{P}\right)_x = -3\alpha^2\overline{(\bar{u}_x(\overline{\rho u})_x)_x}, \tag{8.21b}$$

$$\overline{\rho e}_t + \left(\overline{\rho e}\bar{u} + \bar{u}\bar{P}\right)_x = -3\alpha^2\overline{\left(\bar{u}_x\left((\overline{\rho e})_x + \overline{P}_x\right)\right)_x}. \tag{8.21c}$$

The same pseudospectral method is used to solve equations (8.21). Again an adaptive Runge–Kutta is used to advance in time with all spatial derivatives and the inversion of the Helmholtz operator conducted in the Fourier domain. The simulations were

conducted with $2^{14} = 65536$ grid points on the domain $[0, 2\pi]$ for approximately 10000 time steps. Numerical runs were conducted for values $\alpha = 0.10, 0.09, \ldots, 0.02, 0.01$. The same long-term instability was found in these numerical simulations and was again controlled by setting wave modes higher than $\frac{N}{3}$ to zero every 200 time steps.

8.6. Numerical results. Again the preferred example problem is the shock tube or Riemann problem. The classic Sod test problem [38] is the ideal example as it produces a demonstration of expansion waves, shocks, and contact surfaces, the three classical behaviors of the Riemann problem in the Euler equations. It is also a quite well-known example that is commonly used. For this example the initial conditions are

$$u_0(x) = 0, \tag{8.22a}$$

$$\rho_0(x) = \begin{cases} 1, & 0 < x \leq \pi, \\ 0.125, & \pi < x \leq 2\pi, \end{cases} \tag{8.22b}$$

$$P_0(x) = \begin{cases} 10, & 0 < x \leq \pi, \\ 1, & \pi < x \leq 2\pi. \end{cases} \tag{8.22c}$$

The difficulty with this example is that the boundary conditions are not periodic. As such, we restrict ourselves to the domain $[\frac{\pi}{2}, \frac{3\pi}{2}]$ up to time $t = 0.25$ to avoid contamination regions due to the periodic nature of the simulation.

Again we note that in our previous work, we established that for the CFB equations (1.1) initial conditions with discontinuities were excluded in order to avoid non-entropic behavior [5]. By averaging the initial conditions it was proven that the solution to the CFB equations would be regularized for all time. This was done by averaging the initial conditions with the same filter used on the velocity. We use the same approach here. Thus when the filter is applied to the entire system to obtain equations (8.21), the initial conditions are filtered twice with the same filter used on the equations.

Figures 8.1 and 8.2 show simulations of the observable Euler equations for two different values of α plotted against the solution to the Euler equations. The expansion wave, contact surface, and the shock are all captured in the behavior of the observable Euler equations. For the smaller value of α, the behavior of the observable Euler equations matches that of the Euler equations more closely.

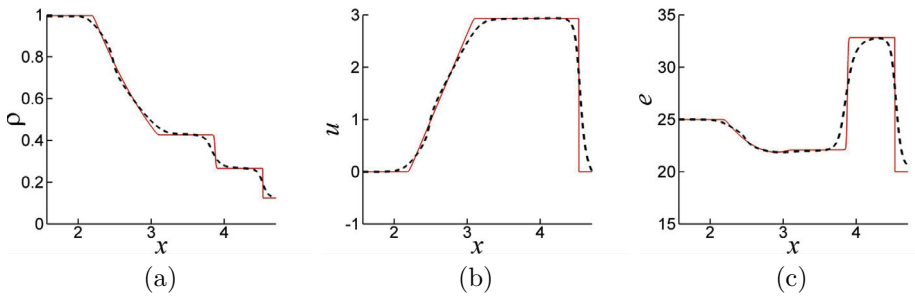

(a) (b) (c)

FIG. 8.1. *A numerical simulation of the observable Euler equations (dashed line) plotted against the solution to the Euler equations (solid line). Here $\alpha = 0.05$ at time $t = 0.25$. In the figures, it is clear that the observable Euler equations are capturing the expansion wave, contact surface, and shock behavior.* (a) *The density.* (b) *The velocity.* (c) *The energy.*

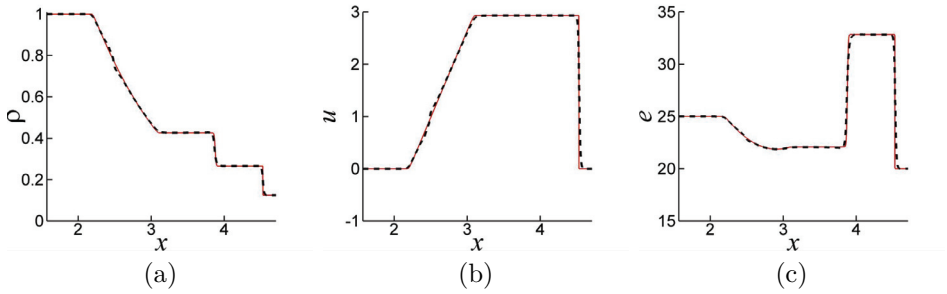

(a) (b) (c)

FIG. 8.2. *A numerical simulation of the observable Euler equations (dashed line) plotted against the solution to the Euler equations (solid line). Here* $\alpha = 0.01$ *at time* $t = 0.25$. *In the figures, it is clear that the observable Euler equations are capturing the expansion wave, contact surface, and shock behavior. With the lower value of* α *the fit is much closer.* (a) *The density.* (b) *The velocity.* (c) *The energy.*

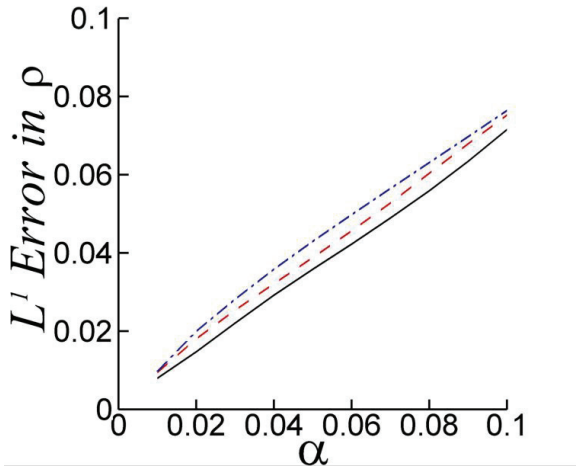

FIG. 8.3. *The difference between the density in solutions of the observable Euler equations and the solution of the Euler equations in the* L^1 *norm as* $\alpha \to 0$. *As* $\alpha \to 0$ *the difference in the solutions also approaches zero. The measurements were taken for* $\alpha = 0.01, 0.02, \ldots, 0.1$ *at times* $t = 0.05$ *(solid line),* $t = 0.15$ *(dashed line), and* $t = 0.25$ *(dashed dotted line).*

As before, we check the convergence of the solutions of the observable Euler equations to the solution of the Euler equations as $\alpha \to 0$. Figures 8.3, 8.4, and 8.5 show that as $\alpha \to 0$ the error in the L^1 norm appears to be approaching zero for the example problem. This suggests that the solutions of the observable Euler equations converge to the solutions of the Euler equations.

8.7. Kinetic energy rates. As in section 7.8, we examine the kinetic energy for the shock tube problem. Again for the shock tube problem, the solutions to the Euler equations are self-similar, depending only on the variable $\frac{x}{t}$, and thus the kinetic energy changes linearly in time. For the Euler equations, we examine the kinetic energy $\frac{1}{2}\rho u^2$, and for the observable Euler equations we examine an unfiltered kinetic energy $\frac{1}{2}\rho u^2$ and a filtered kinetic energy $\frac{1}{2}\bar{\rho}\bar{u}^2$. Other filtered kinetic energies were also considered, but as in the homentropic case, for this example problem, the

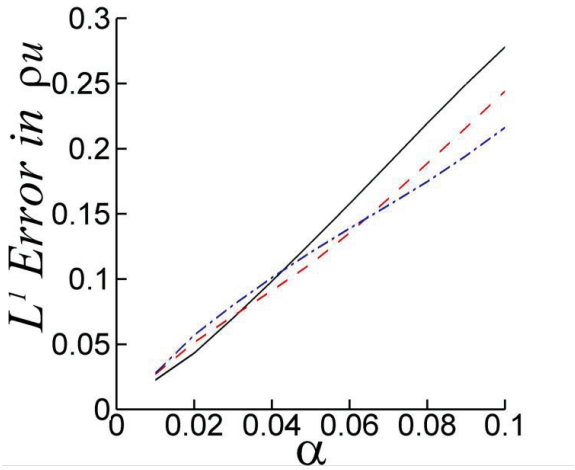

FIG. 8.4. *The difference between the momentum in solutions of the observable Euler equations and the solution of the Euler equations in the* L^1 *norm as* $\alpha \to 0$. *As* $\alpha \to 0$ *the difference in the solutions also approaches zero. The measurements were taken for* $\alpha = 0.01, 0.02, \ldots, 0.1$ *at times* $t = 0.05$ *(solid line),* $t = 0.15$ *(dashed line), and* $t = 0.25$ *(dashed dotted line).*

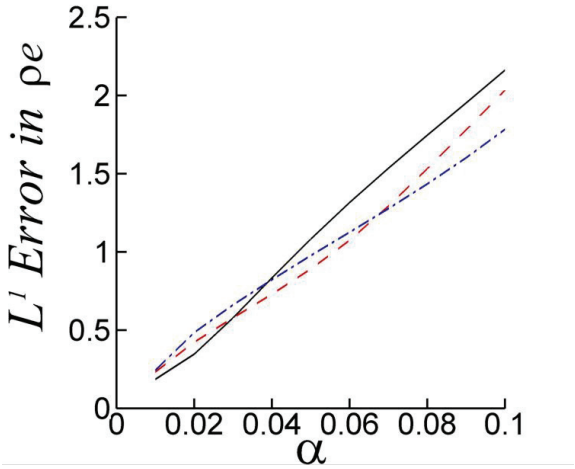

FIG. 8.5. *The difference between the energy in solutions of the observable Euler equations and the solution of the Euler equations in the* L^1 *norm as* $\alpha \to 0$. *As* $\alpha \to 0$ *the difference in the solutions also approaches zero. The measurements were taken for* $\alpha = 0.01, 0.02, \ldots, 0.1$ *at times* $t = 0.05$ *(solid line),* $t = 0.15$ *(dashed line), and* $t = 0.25$ *(dashed dotted line).*

differences between them and $\frac{1}{2}\bar{\rho}\bar{u}^2$ were negligible.

Figure 8.6 shows how the kinetic energies for the observable Euler equations behave for various values of α. Again after a brief period, the energies seem to vary linearly with time. We attribute this brief period to the averaging of the initial conditions. As α decreases the energies for the observable Euler equations approach the energy of the Euler equations, as we would expect if the solutions are converging as $\alpha \to 0$.

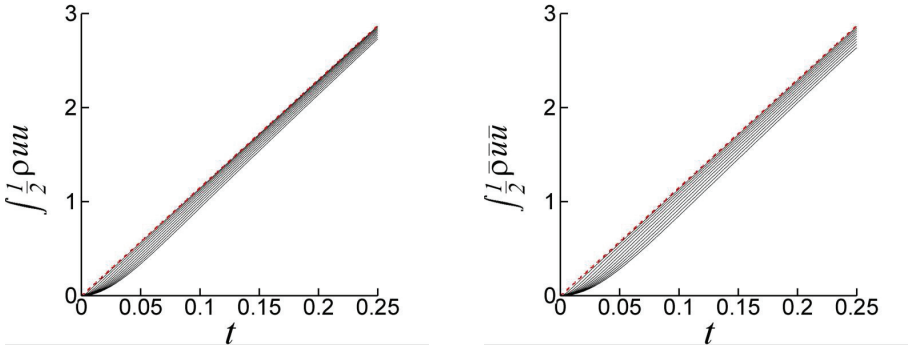

(a) (b)

FIG. 8.6. *The kinetic energy of the Euler equations and the observable Euler equations. The energy for the true solution of the Euler equations is shown as a dashed line. The simulations of the observable Euler equations for* $\alpha = 0.01, 0.02, \ldots, 0.1$ *are shown as solid lines. The bottommost line represents* $\alpha = 0.1$*. As* α *decreases the energy approaches the energy of the Euler equations.* (a) *Plots of the unfiltered kinetic energies,* $\frac{1}{2}\rho u^2$*.* (b) *Plots of the filtered kinetic energies,* $\frac{1}{2}\bar{\rho}\bar{u}^2$*. When examined, the plots of* $\frac{1}{2}\overline{\rho u}\bar{u}$ *and* $\frac{\overline{\rho u}^2}{2\bar{\rho}}$ *were identical to this one.*

9. Conclusion. Using the convectively filtered Burgers (CFB) equations as inspiration, we developed a new averaging technique with the intent of regularizing both shocks and turbulence simultaneously. This paper examines primarily the shock regularization aspect of the technique. We discussed the physical motivation for the method and then derived a general technique to be used on conservation laws. It was then established that this technique, when applied to conservation laws, would preserve the original conservative properties and create similar, if not identical, shock speeds.

The remainder of the paper then examined the effects when this method was applied to the homentropic Euler and Euler equations. The results show much promise. It was found that with the Helmholtz filter both the observable homentropic Euler and observable Euler equations can be rewritten in conservation form, reiterating that the original conservative properties are preserved. For both sets of equations we were able to find traveling shock solutions, where the Rankine–Hugoniot jump conditions for the modified equations reduced to the same jump conditions as for the original equations. For both sets of equations it was proven that as the filtering is decreased, $\alpha \to 0$, the solutions will converge to weak solutions of the original equations. Both of these results show that the proper shock speeds of the original equations will be preserved with the averaging techniques.

Numerical simulations were run on both sets of equations for the shock tube problem. These simulations demonstrated that the modified equations mimic the behavior of the original equations. The observable homentropic Euler equations captured both the expansion wave and the shock front behavior, while the observable Euler equations captured the expansion wave, contact surface, and the shock front. The solutions appeared continuous and smooth. Furthermore, as $\alpha \to 0$ these solutions were seen to be converging to the solutions of the original equations.

There is still more work to be done regarding these equations. It would be beneficial to establish more theory regarding both sets of equations. Specifically existence proofs would be beneficial. It would be interesting to see if either set of equations possesses a Hamiltonian structure.

The observable homentropic Euler and observable Euler equations are showing promise as a potentially new regularization method based on the preliminary examination considered here. From these results we believe that this averaging technique leads to a regularization of the homentropic Euler and Euler equations that is capable of capturing the relevant behavior of the equations. We now list potential future work regarding these equations.

10. Future work. There are many open questions left regarding the observable Euler equations. We have touched on a couple of them, but in this section we list explicitly some of the more pertinent questions.

- *Positivity of density.* In sections 5, 7.1, and 8.1 we addressed the fact that the quantities preserved by the original conservation laws will still be conserved under the modified equations. However, the positivity of the density, ρ, was not addressed. From a physical standpoint a negative density is disallowed, but there is no guarantee that the averaged equations would satisfy this property.
- *Existence of solutions.* As of publication there is currently no rigorous proof for the existence of solutions to the observable homentropic Euler equations (7.2) or the observable Euler equations (8.2) for $\alpha > 0$. Clearly this is desired in order to advance the theory and application of these equations.
- *Compactness of solutions.* In order to show convergence of a subsequence of the solutions, one must first establish the compactness of the function space where the solutions reside. This is often the most challenging part for nonlinear PDEs. It is hoped that with the existence proof would come a priori bounds on the solution which could be utilized to established compactness.
- *Entropy solution.* In this paper we have shown that a converging sequence of bounded solutions will converge to a weak solution of the original equations. A weak solution, however, is not guaranteed to capture the physical behavior desired by the solution. A conservation law will often support multiple, if not an infinite number of, solutions. Thus it is desirable to prove that the solutions are converging to the entropy solution, which is a unique weak solution that reflects the physical behavior of the conservation laws.
- *Multiple dimensions.* For use in practical applications this technique should be extended into two and three dimensions. We believe that the derivation of these equations shown by Mohseni [30] is the proper way to extend this technique into higher dimensions. This is an active direction of current research.

It will be important to address these and other questions in order to establish this averaging method as a valid regularization technique.

Appendix A. Eigenvalues for the observable homentropic Euler equations. This appendix examines how the proposed averaging affects the eigenvalues of the system and thus the characteristic speeds. Again these calculations are important in verifying that the characteristic nature of the homentropic Euler equations is preserved and in establishing numerical stability.

In order to cast the equations in vector-matrix form we first rewrite the equations in their primitive variable form:

$$\rho_t + \bar{\rho} u_x + \bar{u} \rho_x = 0, \tag{A.1a}$$

$$u_t + \bar{u} u_x + \underbrace{\left(\frac{\overline{\rho u} - u\bar{\rho}}{\rho} \right)}_{\beta} u_x + \frac{\gamma \rho^{\gamma - 1}}{\rho} \rho_x = 0. \tag{A.1b}$$

The equations can then be written in vector-matrix form, leading to

$$\begin{bmatrix} \rho \\ u \end{bmatrix}_t + \underbrace{\begin{bmatrix} \bar{u} & \bar{\rho} \\ \frac{a^2}{\rho} & \bar{u}+\beta \end{bmatrix}}_{A} \begin{bmatrix} \rho \\ u \end{bmatrix}_x = 0. \tag{A.2}$$

The eigenvalues of matrix A are

$$\lambda^{\pm} = \bar{u} + \frac{\beta}{2} \pm \sqrt{\frac{\beta^2}{4} + a^2 \frac{\bar{\rho}}{\rho}}. \tag{A.3}$$

Examining quantities β and $\frac{\bar{\rho}}{\rho}$ it seems apparent that as the filtering decreases $\beta \to 0$ and $\frac{\bar{\rho}}{\rho} \to 1$, thus regaining the original eigenvalues.

The matrix A can also be diagonalized and can thus be written in the form

$$A = Q \Lambda Q^{-1}, \tag{A.4}$$

where Λ is a diagonal matrix with its diagonal entries being $\lambda^{\pm}$. Using this we can write the observable homentropic Euler equations in the characteristic form

$$\frac{\partial \mathbf{v}}{\partial t} + \Lambda \frac{\partial \mathbf{v}}{\partial x} = 0, \tag{A.5}$$

where

$$d\mathbf{v} = Q^{-1} \begin{bmatrix} d\rho \\ du \end{bmatrix}. \tag{A.6}$$

By diagonalizing A we find that

$$Q^{-1} = \begin{bmatrix} 1 & \dfrac{\rho\,\beta + \sqrt{\rho\,(\rho\,\beta^2 + 4\,a^2\,\bar{\rho})}}{2\,a^2} \\ 1 & \dfrac{\rho\,\beta - \sqrt{\rho\,(\rho\,\beta^2 + 4\,a^2\,\bar{\rho})}}{2\,a^2} \end{bmatrix}. \tag{A.7}$$

And thus we can define the quantities $v^{\pm}$ through the relation

$$dv^{\pm} = d\rho + \frac{\rho\,\beta \pm \sqrt{\rho\,(\rho\,\beta^2 + 4\,a^2\,\bar{\rho})}}{2\,a^2}\,du. \tag{A.8}$$

We can then say that $dv^{\pm} = 0$ along the characteristic $dx = \lambda^{\pm}\,dt$.

If $\alpha = 0$, there would be no filtering and $\beta = 0$. In this case we would get

$$dv^{\pm} = d\rho \pm \frac{\rho}{a}\,du = 0 \quad \text{along the characteristic } dx = u \pm a\,dt, \tag{A.9}$$

which is the case for the homentropic Euler equations. For the homentropic Euler equations the characteristic variables are able to be computed analytically and are

$$v^{\pm} = u \pm \frac{2a}{\gamma - 1}. \tag{A.10}$$

For nonzero α's there appears to be no straightforward way of integrating (A.8). Thus currently we have no analytical expression for the characteristic variables, though we have not spent much time investigating this possibility.

Appendix B. Eigenvalues for the observable Euler equations. In this appendix we examine the eigenvalues of the observable Euler equations. We begin with equations (8.2), and through substitution and manipulation we can express them in primitive variable form as

$$\rho_t + \bar{u}\rho_x + \bar{\rho}u_x = 0, \tag{B.1}$$

$$u_t + \bar{u}u_x + \underbrace{\left(\frac{\overline{\rho u} - u\bar{\rho}}{\rho}\right)}_{\beta} u_x + P_x = 0, \tag{B.2}$$

$$P_t - (\gamma-1)\beta\rho u u_x + \underbrace{\left((\gamma-1)\bar{P} + (\gamma-1)\overline{\rho e} - \frac{1}{2}(\gamma-1)\bar{\rho}u^2\right)}_{\rho\tilde{a}^2} u_x + (\gamma\bar{u} - (\gamma-1)u)P_x = 0. \tag{B.3}$$

The equations can then be written in vector-matrix form, leading to

$$\begin{bmatrix} \rho \\ u \\ P \end{bmatrix}_t + \underbrace{\begin{bmatrix} \bar{u} & \bar{\rho} & 0 \\ 0 & \beta + \bar{u} & \frac{1}{\rho} \\ 0 & -(\gamma-1)\beta\rho u + \rho\tilde{a}^2 & \gamma\bar{u} - (\gamma-1)u \end{bmatrix}}_{A} \begin{bmatrix} \rho \\ u \\ P \end{bmatrix}_x = 0. \tag{B.4}$$

Define the quantities β, κ, and $\tilde{a}$ as

$$\beta = \frac{\overline{\rho u} - u\bar{\rho}}{\rho}, \tag{B.5}$$

$$\kappa = \bar{u} - u, \tag{B.6}$$

$$\tilde{a}^2 = \frac{\left((\gamma-1)\bar{P} + (\gamma-1)\overline{\rho e} - \frac{1}{2}(\gamma-1)\bar{\rho}u^2\right)}{\rho}. \tag{B.7}$$

Then the eigenvalues of matrix A are

$$\lambda_0 = \bar{u}, \tag{B.8}$$

$$\lambda_\pm = \frac{u+\bar{u}}{2} + \frac{\beta}{2} - \frac{\gamma\kappa}{2} \pm \sqrt{\frac{\beta^2}{4} + \frac{(\gamma-1)^2\kappa^2}{4} - \frac{(\gamma-1)(\bar{u}+u)\beta}{2} + \tilde{a}^2}. \tag{B.9}$$

The quantities β and κ would appear to limit to zero as $\alpha \to 0$, and the quantity $\tilde{a}^2$ would appear to limit to a^2, the speed of sound for the Euler equations. Again the averaging technique alters the eigenvalues, but with the original values regained with the limit as $\alpha \to 0$.

Much like in the homentropic case the matrix A can be diagonalized and thus written in the form $A = Q\Lambda Q^{-1}$. Using this we can write the observable Euler equations in the characteristic form

$$\frac{\partial \mathbf{v}}{\partial t} + \Lambda\frac{\partial \mathbf{v}}{\partial x} = 0, \tag{B.10}$$

where

$$d\mathbf{v} = Q^{-1}\begin{bmatrix} d\rho \\ du \\ dP \end{bmatrix}. \tag{B.11}$$

When diagonalizing A we calculated

$$Q^{-1} = \begin{bmatrix} \frac{\tilde{a}^2-(\gamma-1)\bar{u}\beta}{(\gamma-1)\kappa\bar{\rho}} & 1 & \frac{-1}{\rho(\gamma-1)\kappa} \\ 0 & 1 & \frac{(\gamma-1)\kappa-\beta+\sqrt{\beta^2+(\gamma-1)^2\kappa^2-2(\gamma-1)(\bar{u}+u)\beta+4\tilde{a}^2}}{2\rho(\tilde{a}^2-(\gamma-1)u\beta)} \\ 0 & 1 & \frac{(\gamma-1)\kappa-\beta-\sqrt{\beta^2+(\gamma-1)^2\kappa^2-2(\gamma-1)(\bar{u}+u)\beta+4\tilde{a}^2}}{2\rho(\tilde{a}^2-(\gamma-1)u\beta)} \end{bmatrix}. \tag{B.12}$$

With Q^{-1} containing such a complex structure we were not able to find a straightforward way of determining an analytical expression for the characteristic variables.

Acknowledgment. We would like to thank Dr. Keith Julien for his advice in the numerical simulations.

REFERENCES

[1] K. Mohseni, H. Zhao, and J. Marsden, *Shock regularization for the Burgers equation*, in Proceedings of the 44th AIAA Aerospace Sciences Meeting and Exhibit, American Institute of Aeronautics and Astronautics, Reston, VA, 2006, paper 2006-1516.

[2] G. Norgard and K. Mohseni, *A regularization of the Burgers equation using a filtered convective velocity*, J. Phys. A, 41 (2008), article 344016. Preprint available from http://arxiv.org/abs/0806.0400.

[3] H. S. Bhat and R. C. Fetecau, *A Hamiltonian regularization of the Burgers equation*, J. Nonlinear Sci., 16 (2006), pp. 615–638.

[4] H. S. Bhat and R. C. Fetecau, *Stability of fronts for a regularization of the Burgers equation*, Quart. Appl. Math., 66 (2008), pp. 473–496.

[5] G. Norgard and K. Mohseni, *On the convergence of the convectively filtered Burgers equation to the entropy solution of the inviscid Burgers equation*, Multiscale Model. Simul., 7 (2009), pp. 1811–1837. Preprint available from http://arxiv.org/abs/0805.2176.

[6] D. D. Holm and M. F. Staley, *Wave structure and nonlinear balances in a family of evolutionary PDEs*, SIAM J. Appl. Dyn. Syst., 2 (2003), pp. 323–380.

[7] Y. S. Pavlova, *Convergence of the Leray α-regularization scheme for discontinuous entropy solutions of the inviscid Burgers equation*, Univ. California Undergrad. Res. J., 9 (2006), pp. 27–41.

[8] G. J. Norgard, *Shock Regularization of Conservation Laws through Use of Spatial Averaging in Nonlinear Terms*, Ph.D. thesis, University of Colorado, Boulder, CO, 2009.

[9] A. Cheskidov, D. D. Holm, E. Olson, and E. S. Titi, *On a Leray-α model of turbulence*, Proc. R. Soc. Lond. Ser. A Math. Phys. Eng. Sci., 461 (2004), pp. 629–649.

[10] C. Foias, D. D. Holm, and E. S. Titi, *The Navier-Stokes-α model of fluid turbulence*, Phys. D, 152/153 (2001), pp. 505–519.

[11] J. E. Marsden and S. Shkoller, *Global well-posedness for the Lagrangian averaged Navier-Stokes (LANS-α) equations on bounded domains*, R. Soc. Lond. Trans. Ser. A Math. Phys. Eng. Sci., 359 (2001), pp. 1449–1468.

[12] K. Mohseni, B. Kosović, S. Shkoller, and J. E. Marsden, *Numerical simulations of the Lagrangian averaged Navier-Stokes (LANS-α) equations for homogeneous isotropic turbulence*, Phys. Fluids, 15 (2003), pp. 524–544.

[13] K. Mohseni and H. Zhao, *A dynamic procedure for the Lagrangian averaged Navier-Stokes-α model of turbulent flows*, in Proceedings of the 43rd AIAA Aerospace Sciences Meeting and Exhibit, American Institute of Aeronautics and Astronautics, Reston, VA, 2005, paper 2005-0501.

[14] H. Zhao and K. Mohseni, *A dynamic model for the Lagrangian averaged Navier-Stokes-α equations*, Phys. Fluids, 17 (2005), article 075106.

[15] D. D. Holm, J. E. Marsden, and T. S. Ratiu, *Euler-Poincaré models of ideal fluids with nonlinear dispersion*, Phys. Rev. Lett., 349 (1998), pp. 4173–4177.

[16] S. Y. Chen, C. Foias, D. D. Holm, E. Olson, E. S. Titi, and S. Wynne, *Camassa-Holm equations as a closure model for turbulent channel and pipe flow*, Phys. Rev. Lett., 81 (1998), pp. 5338–5341.

[17] A. A. Ilyin, E. M. Lunasin, and E. S. Titi, *A modified Leray-α subgrid scale model of turbulence*, Nonlinearity, 19 (2006), pp. 879–897.

[18] C. Bardos, J. S. Linshiz, and E. S. Titi, *Global regularity for a Birkhoff-Rott-α approximation of the dynamics of vortex sheets of the $2D$ Euler equations*, Phys. D, 237 (2008), pp. 1905–1911.

[19] D. D. Holm, M. Nitsche, and V. Putkaradze, *Euler-alpha and vortex blob regularization of vortex filament and vortex sheet motion*, J. Fluid Mech., 555 (2006), pp. 149–176.

[20] J. S. Linshiz and E. S. Titi, *Analytical study of certain magnetohydrodynamic-α models*, J. Math. Phys., 48 (2007), article 065504.

[21] Y. Cao, Z. H. Musslimani, and E. S. Titi, *Nonlinear Schroedinger-Helmholtz equation as numerical regularization of the nonlinear Schroedinger equation*, Nonlinearity, 21 (2008), pp. 879–898.

[22] V. V. Chepyzhov, E. S. Titi, and M. I. Vishik, *On the convergence of solutions of the Leray-α model to the trajectory attractor of the $3d$ Navier-Stokes system*, Discrete Contin. Dyn. Syst., 17 (2007), pp. 481–500.

[23] G. Norgard and K. Mohseni, *An examination of the homentropic Euler equations with averaged characteristics*, J. Differential Equations, 248 (2010), pp. 574–593. Preprint available from http://arxiv.org/abs/0902.4729.

[24] H. S. Bhat and R. C. Fetecau, *Lagrangian averaging for the $1D$ compressible Euler equations*, Discrete Contin. Dyn. Syst., 6 (2006), pp. 979–1000.

[25] H. S. Bhat, R. C. Fetecau, and J. Goodman, *A Leray-type regularization for the isentropic Euler equations*, Nonlinearity, 20 (2007), pp. 2035–2046.

[26] H. S. Bhat, R. C. Fetecau, J. E. Marsden, K. Mohseni, and M. West, *Lagrangian averaging for compressible fluids*, Multiscale Model. Simul., 3 (2005), pp. 818–837.

[27] P. Bradshaw, *Turbulence*, Springer-Verlag, Berlin, 1976.

[28] R. H. Kraichnan, *Lagrangian-history statistical theory for Burgers' equation*, Phys. Fluids, 11 (1968), pp. 265–277.

[29] S. N. Gurbatov, S. I. Simdyankin, E. Aurell, U. Frisch, and G. Toth, *On the decay of Burgers turbulence*, J. Fluid Mech., 344 (1997), pp. 339–374.

[30] K. Mohseni, *Derivation of regularized Euler equations from basic principles*, in Proceedings of the AIAA Modeling and Simulation Technologies Conference, American Institute of Aeronautics and Astronautics, Reston, VA, 2009, paper 2009-5695.

[31] C. B. Laney, *Computational Gasdynamics*, Cambridge University Press, Cambridge, UK, 1998.

[32] J. K. Hunter and B. Nachtergaele, *Applied Analysis*, World Scientific, River Edge, NJ, 2001.

[33] J. Duoandikoetxea, *Fourier Analysis*, AMS, Providence, RI, 2000.

[34] C. Canuto, M. Y. Hussaini, A. Quarteroni, and T. A. Zang, *Spectral Methods in Fluid Dynamics*, Springer Ser. Comput. Phys., Springer-Verlag, Berlin, 1988.

[35] M. Germano, U. Piomelli, P. Moin, and W. H. Cabot, *A dynamic subgrid scale eddy viscosity model*, Phys. Fluids A, 3 (1991), pp. 1760–1765.

[36] K. Mohseni, B. Kosovic, J. Marsden, and S. Shkoller, *Numerical simulations of forced homogeneous turbulence using the Lagrangian averaged Navier-Stokes equations*, in Proceedings of the 15th AIAA Computational Fluid Dynamics Conference, American Institute of Aeronautics and Astronautics, Reston, VA, 2001, paper 2001–2645.

[37] H. S. Bhat, *A Hamiltonian Regularization of the Burgers Equation*, Ph.D. thesis, California Institute of Technology, Pasadena, CA, 2005.

[38] G. A. Sod, *A survey of several finite-differences methods from systems of nonlinear hyperbolic conservation laws*, J. Comput. Phys., 27 (1978), pp. 1–31.